Inorganic Chemistry
Article
pubs.acs.org/IC

Trends in Syntheses, Structures, and Properties for Three Series of Ammine Rare-Earth Metal Borohydrides, $M(BH_4)_3 \cdot nNH_3$ (M = Y, Gd, and Dy)

Lars H. Jepsen,[†] Morten B. Ley,[†] Radovan Černý,[‡] Young-Su Lee,[§] Young Whan Cho,[§] Dorthe Ravnsbæk,[∥] Flemming Besenbacher,[⊥] Jørgen Skibsted,[#] and Torben R. Jensen[*,†]

[†]Center for Materials Crystallography, Interdisciplinary Nanoscience Center and Department of Chemistry, Aarhus University, Langelandsgade 140, 8000 Aarhus C, Denmark

[‡]Laboratory of Crystallography, DQMP, University of Geneva, 1211 Geneva, Switzerland

[§]High Temperature Energy Materials Research Center, Korea Institute of Science and Technology, Seoul 136-791, Republic of Korea

[∥]Department of Physics, Chemistry and Pharmacy, University of Southern Denmark, Campusvej 55, Odense M 5230, Denmark

[⊥]Interdisciplinary Nanoscience Center (iNANO) and Department of Physics and Astronomy, Aarhus University, Ny Munkegade 120, Aarhus C 8000, Denmark

[#]Instrument Centre for Solid-State NMR Spectroscopy, Department of Chemistry, and Interdisciplinary Nanoscience Center (iNANO), Aarhus University, Langelandsgade 140, Aarhus C 8000, Denmark

Supporting Information

ABSTRACT: Fourteen solvent- and halide-free ammine rare-earth metal borohydrides $M(BH_4)_3 \cdot nNH_3$, M = Y, Gd, Dy, n = 7, 6, 5, 4, 2, and 1, have been synthesized by a new approach, and their structures as well as chemical and physical properties are characterized. Extensive series of coordination complexes with systematic variation in the number of ligands are presented, as prepared by combined mechanochemistry, solvent-based methods, solid–gas reactions, and thermal treatment. This new synthesis approach may have a significant impact within inorganic coordination chemistry. Halide-free metal borohydrides have been synthesized by solvent-based metathesis reactions of $LiBH_4$ and MCl_3 (3:1), followed by reactions of $M(BH_4)_3$ with an excess of NH_3 gas, yielding $M(BH_4)_3 \cdot 7NH_3$ (M = Y, Gd, and Dy). Crystal structure models for $M(BH_4)_3 \cdot nNH_3$ are derived from a combination of powder X-ray diffraction (PXD), ^{11}B magic-angle spinning NMR, and density functional theory (DFT) calculations. The structures vary from two-dimensional layers (n = 1), one-dimensional chains (n = 2), molecular compounds (n = 4 and 5), to contain complex ions (n = 6 and 7). NH_3 coordinates to the metal in all compounds, while BH_4^- has a flexible coordination, i.e., either as a terminal or bridging ligand or as a counterion. $M(BH_4)_3 \cdot 7NH_3$ releases ammonia stepwise by thermal treatment producing $M(BH_4)_3 \cdot nNH_3$ (6, 5, and 4), whereas hydrogen is released for $n \leq 4$. Detailed analysis of the dihydrogen bonds reveals new insight about the hydrogen elimination mechanism, which contradicts current hypotheses. Overall, the present work provides new general knowledge toward rational materials design and preparation along with limitations of PXD and DFT for analysis of structures with a significant degree of dynamics in the structures.

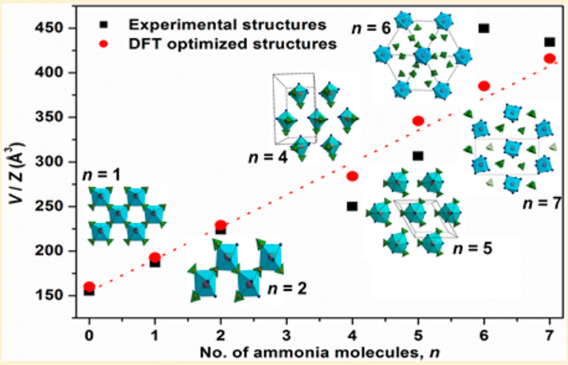

1. INTRODUCTION

The society of today faces a number of challenges concerning a transition toward sustainability with closed cycles for all materials that we use and with an environmentally friendly energy system. Several new solutions are needed and expected to grow from materials science. Hence, new knowledge and synthesis methods allowing rational materials design with desired properties are required. In this field a versatile energy carrier system, e.g., based on hydrogen, enabling renewable energy for mobility applications has received considerable attention. In particular, light element hydrides based on boron or nitrogen are considered as potential solid-state hydrogen storage materials.[1−4]

Metal borohydrides are a fascinating class of materials with surprisingly diverse compositions, structural chemistries, and properties.[5] For example, the γ-$Mg(BH_4)_2$ polymorph is highly porous with the ability to adsorb smaller molecules such as nitrogen and hydrogen.[6] $LiM(BH_4)_3Cl$ (M = Ce, La, and Gd) exhibit high lithium-ion conductivity,[7−9] while $Re(BH_4)_2(THF)_2$ (Re = Eu and Yb) are highly luminescent.[10] Very recently, a series of new perovskites has been reported with tunable optical,

Received: April 28, 2015
Published: July 21, 2015

DOI: 10.1021/acs.inorgchem.5b00951
Inorg. Chem. 2015, 54, 7402−7414

electronic, and magnetic properties combined with the ability for storage of significant amounts of hydrogen.[11]

Metal borohydrides, as hydrogen storage materials, often suffer from poor kinetic or thermodynamic properties, resulting in high temperatures and pressures being required for hydrogen release and uptake, which hampers their utilization as hydrogen storage materials. Ammine metal borohydrides, $M(BH_4)_m{\cdot}nNH_3$ have received significant attention owing to the favorable dihydrogen interaction between partly positively charged hydrogen, $H^{\delta+}$, bonded to N and partly negatively charged hydrogen, $H^{\delta-}$, bonded to B, which may result in a lower temperature for elimination of hydrogen molecules. Among the most promising materials are $Zn(BH_4)_2{\cdot}2NH_3$ and $Li_2Al(BH_4)_5{\cdot}6NH_3$ that release up to 10 wt % H_2 with high purity (>99%) below 120 °C.[12,13] The first ammine rare-earth metal borohydride, $Y(BH_4)_3{\cdot}4NH_3$, was described recently,[14] and it was found to release more than 8.7 wt % H_2 with only trace amounts of NH_3 below 200 °C. However, $Y(BH_4)_3{\cdot}4NH_3$ was prepared by mechanochemical treatment of $YCl_3{\cdot}4NH_3$ and $LiBH_4$ (1:3), which also produces LiCl in addition to the desired product. However, LiCl lowers the hydrogen storage capacity in the composite sample, and thus, a new synthesis method providing a pure material is greatly desired. Furthermore, several ammine metal borohydrides remain not fully investigated structurally, chemically, and physically, which has prompted the present investigation. Insight about the correlation between structure and properties such as thermal decomposition mechanism and its relation to dihydrogen bonds may provide important knowledge toward rational design of new useful materials.

In this work, we present a novel approach to prepare halide-free ammine rare-earth metal borohydrides by the synthesis of three series of $M(BH_4)_3{\cdot}nNH_3$ where M = Y, Gd, and Dy and n = 7, 6, 5, 4, 2, and 1. The crystal structures for all of these new compounds are solved using synchrotron radiation powder X-ray diffraction (SR-PXD) in combination with ^{11}B MAS NMR and DFT calculations, and the thermal decompositions are investigated by several complementary experimental techniques.

2. EXPERIMENTAL SECTION

2.1. Synthesis. The samples of $M(BH_4)_3{\cdot}7NH_3$, M = Y, Gd, and Dy, were prepared by similar synthesis schemes, and the samples are denoted s1, s2, and s3, respectively (Table 1). Powders of MCl_3–$LiBH_4$ (1:3) were mechanochemically treated using a Fritz Pulverisette 6 ball mill. The powders and tungsten carbide balls (diameter 10 mm, balls-to-sample mass ratio 30:1) were loaded in a tungsten carbide vial (80 mL) under inert conditions. The powders were ball milled at 250 rpm for 2 min, intervened by a 2 min break, and this sequence was repeated 60 times. In order to complete reaction 1, the ball-milled samples were heated to 190 °C under $p(H_2)$ = 80 bar for 30 min in a stainless steel autoclave, which changed the color of the samples from white to yellow.

$$MCl_3(s) + 3LiBH_4(s) \rightarrow M(BH_4)_3(s) + 3LiCl(s) \qquad (1)$$

Dimethyl sulfide ($S(CH_3)_2$) was added to the mixtures of $M(BH_4)_3$ and LiCl, which dissolves $M(BH_4)_3$, allowing removal of LiCl by filtration.[15] Excess and coordinated $S(CH_3)_2$ was removed by applying vacuum at 140 °C, which gives rise to dry $Gd(BH_4)_3$, $Dy(BH_4)_3$, and a mixture of α-$Y(BH_4)_3$ and β-$Y(BH_4)_3$. $M(BH_4)_3{\cdot}7NH_3$ was formed either by passing dry NH_3 gas through the solution of $M(BH_4)_3$ in $S(CH_3)_2$ or by a reaction between dry NH_3 gas and solid $M(BH_4)_3$ for 2 h at −5 °C. The powders were finally dried under dynamic vacuum at RT for 15 min. The two different routes give rise to the same products, which are all halide and solvent free.

The mixtures of $Y(BH_4)_3{\cdot}7NH_3$–$Y(BH_4)_3$ were prepared by ball milling (BM) in the ratios $Y(BH_4)_3{\cdot}7NH_3$–$Y(BH_4)_3$ 4:3, 3:4, and 1:6 using a Fritz Pulverisette No.4. These samples are denoted s4, s5, and s7, respectively. Additionally, mixtures of s4–$Y(BH_4)_3$ (2:2 and 1:3) were ball-milled and denoted s6 and s8, respectively. The powders were packed in inert atmosphere in a tungsten carbide vial (80 mL) together with tungsten carbide balls and with a ball-to-sample mass ratio of 30:1. The powders were ball-milled for 2 min at 300 rpm, intervened by a 2 min break, and this sequence was repeated 60 times. Sample s1 was heated in a Schlenk tube under argon atmosphere using an oil bath heated to 100, 120, 140, and 165 °C for 2 min, and these samples are denoted s1_100, s1_120, s1_140, and s1_165, respectively.

All samples have been stored at −35 °C in order to avoid ammonia release from the synthesized samples. All sample preparation including ammonia-related procedures was conducted under anaerobic and anhydrous conditions by Schlenk techniques and in an argon-filled glovebox. Notice, NH_3 is extremely toxic and should therefore only be handled in a fume hood with ventilation. The reactants used were anhydrous dysprosium chloride, $DyCl_3$ (Sigma-Aldrich, 99.99%), yttrium chloride, YCl_3 (Sigma-Aldrich, 99.99%), gadolinium chloride, $GdCl_3$ (Sigma-Aldrich, 99.99%), lithium borohydride, $LiBH_4$ (Sigma-Aldrich, 95%), and dry ammonia gas, NH_3 (<33 ppm of H_2O). The solvent used was anhydrous dimethyl sulfide, $S(CH_3)_2$ (Sigma-Aldrich, 99.0%). All chemicals were used as received.

2.2. Characterization. *2.2.1. In-House Laboratory X-ray Diffraction.* PXD measurements were performed in Debye–Scherrer transmission geometry using a Stoe diffractometer equipped with a curved Ge(111) monochromator (Cu Kα1 radiation, λ = 1.54060 Å) and a curved position-sensitive detector. Data were collected at RT between 2θ = 4° and 127° with counting times of 180 s. Air-sensitive samples were mounted in a glovebox in 0.5 mm glass capillaries sealed with glue.

2.2.2. Synchrotron Radiation Powder X-ray Diffraction (SR-PXD). In-situ SR-PXD data were collected for $Y(BH_4)_3{\cdot}7NH_3$ (λ = 0.82712 Å) and s4 (λ = 0.825654 Å) at the I11 beamline at the Diamond synchrotron facility, Oxford, England, with a MythenII detector. The sample was packed in a glass capillary (i.d. 0.5 mm) and heated from RT to 300 °C (5 °C/min). Additionally, in-situ SR-PXD data were collected

Table 1. Synthesized Samples and Compositions

name	reactants	nominal sample composition	products	n/m ratio
s1	$Y(BH_4)_3$ + excess of NH_3	$Y(BH_4)_3{\cdot}7NH_3$	$Y(BH_4)_3{\cdot}7NH_3$	7/3
s2	$Gd(BH_4)_3$ + excess of NH_3	$Gd(BH_4)_3{\cdot}7NH_3$	$Gd(BH_4)_3{\cdot}7NH_3$	7/3
s3	$Dy(BH_4)_3$ + excess of NH_3	$Dy(BH_4)_3{\cdot}7NH_3$	$Dy(BH_4)_3{\cdot}7NH_3$	7/3
s4	$Y(BH_4)_3{\cdot}7NH_3$–$Y(BH_4)_3$ (4:3)[a]	"$Y(BH_4)_3{\cdot}4NH_3$"	$Y(BH_4)_3{\cdot}5NH_3$ + amorphous	4/3
s5	$Y(BH_4)_3{\cdot}7NH_3$–$Y(BH_4)_3$ (3:4)[a]	"$Y(BH_4)_3{\cdot}3NH_3$"	$Y(BH_4)_3{\cdot}4NH_3$ + $Y(BH_4)_3{\cdot}5NH_3$	3/3
s6	s4–$Y(BH_4)_3$ (2:2)[a]	"$Y(BH_4)_3{\cdot}2NH_3$"	α-$Y(BH_4)_3$ + $Y(BH_4)_3{\cdot}4NH_3$	2/3
s7	$Y(BH_4)_3{\cdot}7NH_3$–$Y(BH_4)_3$ (1:6)[a]	"$Y(BH_4)_3{\cdot}1NH_3$"	α-, β-$Y(BH_4)_3$ + $Y(BH_4)_3{\cdot}2NH_3$	1/3
s8	s4–$Y(BH_4)_3$ (1:3)[a]	"$Y(BH_4)_3{\cdot}1NH_3$"	α-, β-$Y(BH_4)_3$ + $Y(BH_4)_3{\cdot}2NH_3$	1/3

[a] The mixtures have been mechanochemically treated.

DOI: 10.1021/acs.inorgchem.5b00951
Inorg. Chem. 2015, 54, 7402−7414

for $Y(BH_4)_3{\cdot}7NH_3$ (λ = 0.772638 Å), s6 (λ = 0.772638 Å), and $Dy(BH_4)_3{\cdot}7NH_3$ (λ = 0.681344 Å) at SNBL, ESRF, Grenoble, France, with a Pilatus area detector. At beamline I711 at the MAX-II synchrotron in the MAX IV laboratory, Lund, Sweden, in-situ SR-PXD data were measured for $Y(BH_4)_3{\cdot}7NH_3$ (λ = 0.99102 Å), $Gd(BH_4)_3{\cdot}7NH_3$ (λ = 0.9904 Å), and s5 (λ = 0.9938 Å) with a MAR165 CCD detector. The sample was packed in a sapphire (Al_2O_3) single-crystal tube (1.09 mm o.d., 0.79 mm i.d.) in an argon-filled glovebox ($p(O_2, H_2O) <$ 0.5 ppm) mounted on a specially designed sample holder.[16] Data were obtained from RT to 200 °C (5 °C/min) under argon atmosphere. In-situ SR-PXD experiments were conducted for $Gd(BH_4)_3{\cdot}6NH_3$ at beamline P02 at Petra III, DESY, Hamburg, Germany, with a PerkinElmer XRD 1621 detector system and wavelength λ = 0.2072 Å. In-situ SR-PXD was measured from RT to 200 °C (5 °C/min) under argon atmosphere.

All obtained raw images were transformed to 2D-powder diffraction patterns using the FIT2D program,[17] which was also used to remove diffraction spots from the single-crystal sapphire tube used as sample holder. The intensities of selected Bragg diffraction peaks were fitted to a Gaussian curve for each diffraction pattern in order to illustrate changes in the sample composition as a function of temperature.

2.2.3. Structural Solution and Refinement. The crystal structures of $M(BH_4)_3{\cdot}nNH_3$ (M = Y, Gd, and Dy; n = 7, 6, 5, 4, 2, and 1) were solved and refined from the SR-PXD data. The general procedure involved indexing of the unit cell using the program DICVOL[18] and subsequently solving the structure by global optimization in direct space, as implemented in the program FOX.[19] The structural model was refined by the Rietveld method using the program Fullprof and checked for higher symmetry using the ADDSYM routine in Platon.[20,21] The results of the final Rietveld refinements are shown in Figures S1−S6, Supporting Information. All Bragg peak positions are in accord with the observed PXD data, which reveals that the crystal system, unit cell parameters, and space group symmetry are correctly determined. However, significant discrepancy between some measured and calculated Bragg peak intensities is observed for $M(BH_4)_3{\cdot}nNH_3$ (n = 5 and 6, Figures S2 and S3, Supporting Information), which suggests structural disorder and/or dynamics in the structures. The disorder/dynamics may be created by large anisotropic vibrations of the BH_4^- tetrahedra, and the determination of B and H atomic positions in BH_4^- is tentative for $M(BH_4)_3{\cdot}nNH_3$, n = 5 and 6. In accord, large thermal elipsoids were obtained for boron by Rietveld refinement for $M(BH_4)_3{\cdot}nNH_3$ (n = 5 and 6).

2.2.4. Density Functional Theory Calculation. The structural models from Rietveld refinement of $Y(BH_4)_3{\cdot}nNH_3$ (n = 7, 6, 5, 4, 2, and 1) of SR-PXD data were further optimized by density functional theory (DFT) calculations. The calculations were performed within the generalized-gradient approximation by Perdew, Burke, and Ernzerhof as implemented in the Vienna Ab-initio Simulation Package (VASP).[22,23] Projector-augmented wave potential with a planewave cutoff energy of 500 eV was used.[24] Regular k-point meshes, which are dense enough to converge total energies within 0.5 meV/fu, were chosen. Structural optimization was performed until the force on each atom became smaller than 0.005 eV/Å. In order to evaluate the stability of the structures, the unit cell parameters were optimized using a higher planewave cutoff energy of 600 eV. When $Y(BH_4)_3{\cdot}nNH_3$ forms a molecular cluster, the van der Waals density functional[25] is included, as implemented in the VASP code,[26] and the results are compared. Optimized structures with experimental cell parameters are provided in the Supporting Information.

2.2.5. ^{11}B NMR Measurements. The $Y(BH_4)_3{\cdot}nNH_3$ samples have been studied by ^{11}B magic-angle spinning (MAS) NMR since the Gd^{3+} and Dy^{3+} ions in the two other ammine metal borohydrides are paramagnetic. ^{11}B MAS NMR spectra have been obtained at 7.05 and 14.09 T on Varian INOVA-300 and Varian Direct-Drive VNMR-600 spectrometers using home-built 7 and 4 mm CP/MAS probes, respectively. The 7.05 T spectra employed an ^{11}B rf field strength of $\gamma B_1/2\pi$ = 41 kHz, a 0.5 μs pulse width, TPPM ^1H decoupling ($\gamma B_2/2\pi$ = 42 kHz), and a 4 s relaxation delay. The variable-temperature ^{11}B MAS NMR experiments used the same setup as described recently for a similar VT-^{11}B MAS NMR study.[27] The 14.09 T spectra were acquired with an ^{11}B rf field strength of $\gamma B_1/2\pi$ = 60 kHz, a 0.5 μs pulse width, TPPM ^1H decoupling ($\gamma B_2/2\pi$ = 50 kHz), and a 10 s relaxation delay. All experiments used airtight end-capped zirconia (PSZ) 4 or 7 mm rotors, packed in an argon-filled glovebox. The determination of the ^{11}B quadrupole coupling parameters (C_Q and η_Q) and isotropic chemical shifts (δ_{iso}) was performed by least-squares fitting of simulated to experimental spectra for the satellite transitions using the STARS software package.[28] The ^{11}B isotropic chemical shifts are in ppm relative to neat $F_3B{\cdot}O(CH_2CH_3)_2$.

2.2.6. Fourier-Transformed Infrared Spectroscopy (FTIR). The samples were characterized by infrared absorption spectroscopy using a NICOLET 380 FT-IR from Thermo Electron Corp. The samples were exposed to air for approximately 15 s when transferred from the sample vial to the instrument.

2.2.7. Thermal Analysis and Mass Spectroscopy. Thermogravimetric analysis (TGA) and differential scanning calorimetry (DSC) were measured using a PerkinElmer STA 6000 coupled with a mass spectrometer (MS) (Hiden Analytical HPR-20 QMS sampling system). Each sample (approximately 5 mg) was placed in an Al_2O_3 crucible and heated from 40 to 400 °C (5 °C/min) with an argon purge rate of 20 mL/min. The outlet gas was monitored for hydrogen, ammonia, diborane, and dimethyl sulfide using mass spectroscopy.

2.2.8. Temperature-Programmed Photographic Analysis (TPPA). Samples of $M(BH_4)_3{\cdot}7NH_3$ (M = Y, Gd, and Dy, approximately 10 mg) were sealed under argon in a glass tube placed in a home-built oven as described recently.[29] The samples were heated from 25 to 300 °C with a heating rate of 3 °C/min, while photos of the sample were collected every 5 s.

3. RESULTS AND DISCUSSION

3.1. Synthesis and Initial Phase Analysis.

Chemical reactions between NH_3(g) and dry, solid $M(BH_4)_3$ (M = Y, Gd, and Dy) are clearly exothermic, and the volumes of the powders increase significantly when reaction 2 takes place. PXD data for $M(BH_4)_3$ (M = Y, Gd, and Dy) reacted with NH_3 at −5 °C are shown in Figure S7, Supporting Information, and all observed reflections can be assigned to $M(BH_4)_3{\cdot}7NH_3$, i.e., the reactants are fully consumed by reaction 2.

$$M(BH_4)_3(s) + 7NH_3(g) \rightarrow M(BH_4)_3{\cdot}7NH_3(s) \qquad (2)$$

PXD and FTIR data have been measured for $Gd(BH_4)_3$ and $Dy(BH_4)_3$ reacted with NH_3 at RT. The gadolinium sample (Figure S8, Supporting Information, left) reveals Bragg reflections from $Gd(BH_4)_3{\cdot}6NH_3$, in accord with sharp FTIR bands in the N−H stretch region (Figure S8, Supporting Information, right). The dysprosium sample contains $Dy(BH_4)_3{\cdot}4NH_3$ and an amorphous material as product. The lower ammonia content for products obtained at RT is ascribed to the significant amount of heat evolved from the exothermic solid−gas reaction eq 2.

Upon thermal treatment, the $M(BH_4)_3{\cdot}7NH_3$ samples stepwise release ammonia, producing $M(BH_4)_3{\cdot}nNH_3$ (n = 6, 5, and 4). In order to tailor the content of ammonia, i.e., to produce $M(BH_4)_3{\cdot}nNH_3$ for $n < 4$, mixtures of $Y(BH_4)_3{\cdot}7NH_3$−$Y(BH_4)_3$ (4:3, s4), $Y(BH_4)_3{\cdot}7NH_3$−$Y(BH_4)_3$ (3:4, s5), s4−$Y(BH_4)_3$ (2:2, s6), $Y(BH_4)_3{\cdot}7NH_3$−$Y(BH_4)_3$ (1:6, s7), and s4−$Y(BH_4)_3$ (1:3, s8) have been mechanochemically treated. PXD data for s4−s8 (Figure S9, Supporting Information, and Table 1) reveal that it is possible to manipulate the NH_3 content by mechanochemical treatment, e.g., $Y(BH_4)_3{\cdot}2NH_3$ is formed for s7 and s8. However, phase-pure samples are not obtained. Furthermore, $Y(BH_4)_3{\cdot}NH_3$ is formed upon thermal treatment of s7 and s8. Thus, the entire series for $Y(BH_4)_3{\cdot}nNH_3$ n = 7, 6, 5, 4, 2, and 1 has been synthesized.

DOI: 10.1021/acs.inorgchem.5b00951
Inorg. Chem. 2015, 54, 7402−7414

Table 2. Structural Data Extracted from Rietveld Refinement for the Series of Compounds $Y(BH_4)_3{\cdot}nNH_3$ (*n* = 7, 6, 5, 4, 2, and 1)[a]

	$Y(BH_4)_3{\cdot}7NH_3$	$Y(BH_4)_3{\cdot}6NH_3$	$Y(BH_4)_3{\cdot}5NH_3$	$Y(BH_4)_3{\cdot}4NH_3$[b]	$Y(BH_4)_3{\cdot}2NH_3$	$Y(BH_4)_3{\cdot}NH_3$
cryst syst	orthorhombic	cubic	hexagonal	orthorhombic	orthorhombic	orthorhombic
space group	$Pca2_1$	$Pa\text{-}3$	$P6_3$	$Pna2_1$	$Pbca$	$Cmc2_1$
T [°C][c]	RT	95	102	162	155	121
a [Å]	14.9569(7)	12.339(5)	8.5476(8)	12.3869(6)	7.6126(1)	7.8755(3)
b [Å]	8.4111(4)			7.1414(4)	12.0774(2)	7.7449(3)
c [Å]	13.8122(6)		9.941(2)	11.5313(5)	19.4662(3)	12.2466(4)
V [Å^3]	1737.6(2)	1878.7(12)	629.0(2)	1020.06(8)	1789.75(4)	747.05(2)
Z	4	4	2	4	8	4
V/Z [Å^3]	434.41	469.77	314.52	255.24	223.72	186.75
M [g/mol]	252.6479	235.6174	218.5869	201.5564	167.495	150.465
ρ (calcd) [g/mL]	0.967	0.833	1.154	1.311	1.243	1.338
$\rho_m(H_2)$ [wt %]	13.17	12.83	12.45	12.00	10.83	10.05
$\rho_v(H_2)$ [kg H_2/m^3]	127.3	106.9	143.7	157.4	134.7	134.4

[a] Similar structural data for $M(BH_4)_3{\cdot}nNH_3$ (M = Gd and Dy; *n* = 7, 6, 5, and 4) are provided in Table S1, Supporting Information. [b] The structure of $Y(BH_4)_3{\cdot}4NH_3$ is a new structural model as compared to ref 14. [c] Temperature for the data collection.

3.2. Crystal Structure Analysis.

All $M(BH_4)_3{\cdot}nNH_3$ ammine metal borohydrides are isostructural for each value of *n* and M = Y, Gd, and Dy similar to $M(BH_4)_3$ (M = Y, Gd, and Dy),[30] most likely as a result of similar cation sizes: $r(Y^{3+}$ = 0.900 Å), $r(Dy^{3+}$ = 0.912 Å), and $r(Gd^{3+}$ = 0.938 Å).[31] All structures are determined for the first time in this work, and a new structural model for *n* = 4 is presented, which contradicts a previously reported stucture.[14] Table 2 provides structural data and hydrogen storage capacities for $Y(BH_4)_3{\cdot}nNH_3$ (*n* = 7, 6, 5, 4, 2 and 1), while data for $M(BH_4)_3{\cdot}nNH_3$ (M = Gd and Dy; *n* = 7, 6, 5, and 4) are presented in Table S1, Supporting Information.

$M(BH_4)_3{\cdot}7NH_3$ (M = Y, Gd, and Dy). $M(BH_4)_3{\cdot}7NH_3$ (M = Y, Gd, and Dy) crystallize in orthorhombic unit cells (space group $Pca2_1$, No. 29) with one unique M^{3+} cation position which is coordinated by seven NH_3, forming a monocapped trigonal prism (Figure 1). The $[Y(NH_3)_7]^{3+}$ prisms form hexagonal patterns in the *ab* plane (Figure 1a), which are stacked in the order *ABAB* along the *c* axis (Figure 1b). Borohydride complex anions, BH_4^-, fill the space between the prisms within and between the *ab* layers and act as counterions in the solid $[M(NH_3)_7](BH_4)_3$. The structural model is stable according to DFT, and the optimized structure agrees well with the experimental diffraction data. DFT structural optimization mainly modifies the orientation of the BH_4^- and NH_3 groups, reveals strong dihydrogen interactions, and decreases the shortest $H^{\delta-}\cdots H^{\delta+}$ contacts to 1.850 Å. This dense network of dihydrogen bonds stabilizes the structure. The unit cell parameters slightly change upon DFT optimization, giving *a* = 14.55 Å, *b* = 8.36 Å, and *c* = 13.86 Å for $Y(BH_4)_3{\cdot}7NH_3$, which suggests good agreement between the experimental and the optimized structural models. A 7-fold coordination in the form of monocapped trigonal $[M(NH_3)_7]^{3+}$ prisms is also found in the RT-polymorph of ZrO_2, baddeleyite,[32] but for Y only in $Y_4O(OH)_9NO_3$.[33] The DFT-optimized Y−N bond lengths vary from 2.47 to 2.50 Å. The structures of $[M(NH_3)_7](BH_4)_3$ are the first reported heptaammine metal borohydrides. The ammine yttrium chloride, $YCl_3{\cdot}7NH_3$, is reported, but the crystal structure remains unknown.[14]

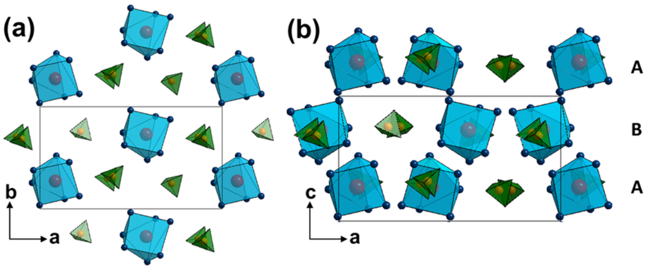

Figure 1. Orthorhombic crystal structure of $M(BH_4)_3{\cdot}7NH_3$ (M = Y, Gd, and Dy) with space group symmetry $Pca2_1$. The structure consists of complex ions $[M(NH_3)_7]^{3+}$ (light blue polyhedra) charge balanced by BH_4^- complex anions (green tetrahedra). M^{3+} (red) coordinates to seven N atoms (blue) in NH_3. (a) $[M(NH_3)_7]^{3+}$ prisms form hexagonal patterns in the *ab* plane, and (b) that stacked in the order *ABAB* along the *c* direction. H atoms are not shown for simplicity.

$M(BH_4)_3{\cdot}6NH_3$ (M = Y, Gd, and Dy). $M(BH_4)_3{\cdot}6NH_3$ (M = Y, Gd, and Dy) crystallize in cubic cells (space group $Pa\text{-}3$, No.205) with the M^{3+} cations octahedrally cordinated by six NH_3 molecules forming octahedral complexes $[M(NH_3)_6]^{3+}$ (Figure 2). The $[M(NH_3)_6]^{3+}$ octahedra are ordered in a hexagonal pattern in (111) layers (Figure 2a), which are stacked in the sequence *ABC* along the [111] direction (Figure 2b). The BH_4^- tetrahedra fill the space between the prisms within and between the (111) layers and act as counterions in the solid $[M(NH_3)_6](BH_4)_3$. The $Pa\text{-}3$ space group symmetry assumes disordered H postions in the BH_4^- groups at 4*b* sites, and the

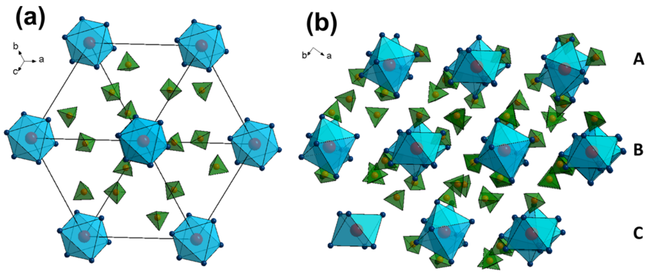

Figure 2. Cubic crystal structure of $M(BH_4)_3{\cdot}6NH_3$ (M = Y, Gd, and Dy) with space group symmetry $Pa\text{-}3$. M^{3+} (red) is octahedrally coordinated by six NH_3 molecules forming a complex $[M(NH_3)_6]^{3+}$ (blue octahedra), while BH_4^- (green tetrahedra) act as counterions. (a) $[M(NH_3)_6]^{3+}$ octahedra form hexagonal patterns in (111) layers, (b) which are stacked in the order *ABC* along the [111] direction. H atoms are not shown for simplicity.

full symmetry cannot be preserved when a specific position is assigned to those H atoms. To perform a static DFT calculation, the symmetry is reduced to $P2_13$ and the atomic positions of Y at 4*a* and B at 4*b* are fixed, while all other positions are optimized. DFT optimization gives a significantly smaller unit cell parameter of a = 11.55 Å, corresponding to a decrease of 6.8% from the experimental value. The energy decreases by 0.48 eV/fu during the optimization process. The lower density of the experimental structure may indicate a high degree of mobility of the BH_4^- anions, which further underlines that a more complex structural model is needed in order to fully describe peak intensities as mentioned in the Experimental Section (section 2.2.3). Thus, a higher entropy may contribute to stabilization of the energetically less favorable experimental structure. As a test, the orientations of the BH_4^- groups at the 8*c* site were changed such that they face the closest Y in a tridentate configuration. The energy increase is small (7 meV/fu), which indicates a flexibility of the BH_4^- groups at the 8*c* and 4*b* sites and high entropy. The structure of $M(BH_4)_3{\cdot}6NH_3$ is an antitype of RT-$(NH_4)_3GaF_6$,[34] which may also be seen as derived from double antiperovskite structure type. The octahedral coordination of Y, Gd, and Dy is similar to the structures of $Mn(BH_4)_2{\cdot}6NH_3$ and $Li_2Mn(BH_4)_4{\cdot}6NH_3$[35] and is common for ammine rare-earth and transition metal halides.

$M(BH_4)_3{\cdot}5NH_3$ (M = Y, Gd, and Dy). $M(BH_4)_3{\cdot}5NH_3$ (M = Y, Gd, and Dy) crystallize in hexagonal unit cells (space group $P6_3$, No. 173) with the M^{3+} cations 8-fold coordinated by five NH_3 molecules and three terminal BH_4^- groups in molecular complexes $[M(NH_3)_5(BH_4)_3]$. The complexes $[M(NH_3)_5(BH_4)_3]$ are packed in the *ab* plane in a hexagonal pattern (Figure 3a), which are stacked in the order *ABAB* along the *c* axis (Figure 3b). The molecular complexes are held together by dihydrogen contacts from BH_4^- and NH_3. The DFT optimization reveals that the three BH_4^- groups coordinate to the metal by corner sharing (η^1), which is rare. Exclusion of the van der Waals energy in the DFT optimization results in approximately 40% expansion of the unit cell volume. This result indicates that molecular complexes are weakly interacting in the solid state. Even after including the van der Waals energy, the structure is still under compression and the optimized unit cell volume is 10% larger than the experimental volume. Generally, BH_4^- complexes often coordinate to metals via edge sharing (η^2), but for $Y(BH_4)_3{\cdot}5NH_3$, limited space in the coordination sphere around yttrium prevents this coordination. In accord, PXD and DFT reveal corner-sharing M−BH_4 coordination. Furthermore, discrepancy between some calculated and observed diffracted intensities (Figure S3, Supporting Information) and relatively large thermal elipsoids for BH_4^- suggests disorder and/or dynamics of BH_4^-. Such disorder/dynamics may be created by a "competition" between more than one possible M−BH_4 coordination, e.g., corner sharing and distorted edge sharing.

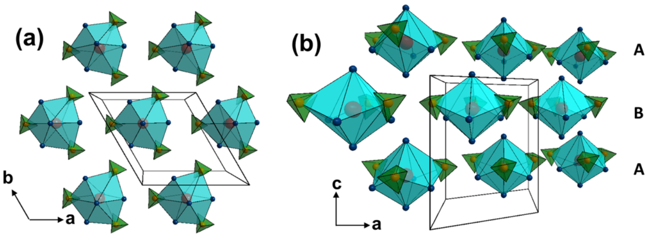

Figure 3. Hexagonal crystal structure of $M(BH_4)_3{\cdot}5NH_3$ (M = Y, Gd, and Dy) with space group symmetry $P6_3$. M^{3+} (red) is coordinated by five N in NH_3 and three BH_4^- (green tetrahedra) forming neutral molecular complexes $[M(NH_3)_5(BH_4)_3]$ (blue octahedra). (a) Molecular complexes are ordered in hexagonal patterns in the *ab* plane, (b) which are stacked in the order *ABAB* along the *c* direction. H atoms are not shown for simplicity.

$M(BH_4)_3{\cdot}4NH_3$ (M = Y, Gd, and Dy). $M(BH_4)_3{\cdot}4NH_3$ (M = Y, Gd, and Dy) crystallize in orthorhombic unit cells (space group $Pna2_1$, No.33). The unit cell parameters of $Y(BH_4)_3{\cdot}4NH_3$, refined using SR-PXD data measured at 162 °C, a = 12.3876(8) Å, b = 7.1401(7) Å, and c = 11.5331(5) Å, and V = 1020.1(2) Å^3, are slightly larger than those previously reported at RT, V = 997.02(2) Å^3.[14] The M^{3+} cations are 7-fold coordinated by four NH_3 and three BH_4^-, creating a neutral molecular complex $[M(NH_3)_4(BH_4)_3]$ (Figure 4). This contradicts the previously reported structural model, which suggests distorted octahedral complexes with one BH_4^- as a counterion.[14] In the previously reported model,[14] the Y−N distances vary unrealistically from 2.28 to 2.93 Å, while they are in a narrow range from 2.44 to 2.49 Å in the new structural model presented here. The molecular complexes $[M(NH_3)_4(BH_4)_3]$ are packed in *ab* layers in a hexagonal pattern (Figure 4a), which are stacked in the order *ABAB* along the *c* axis (Figure 4b) similar to $[M(NH_3)_7]^{3+}$ and $[M(NH_3)_5(BH_4)_3]$ units in the $M(BH_4)_3{\cdot}7NH_3$ and $M(BH_4)_3{\cdot}5NH_3$ structures, respectively. The DFT structural optimization reveals that the three BH_4^- groups coordinate to the metal through edge sharing (η^2). Notice, the previously suggested structural model[14] is energetically less stable by 0.164 meV/fu than the present structure, according to the DFT total energy calculation. Unit cell parameter optimizations with and without inclusion of the van der Waals energy result in 11% or 18% increase compared to the experimental model, which is less dramatic as compared to that obtained for $M(BH_4)_3{\cdot}5NH_3$. For both n = 4 and 5, the molecular complexes are weakly bound together in the solid and the possible structural models from DFT simulations form a relatively flat potential energy surface.

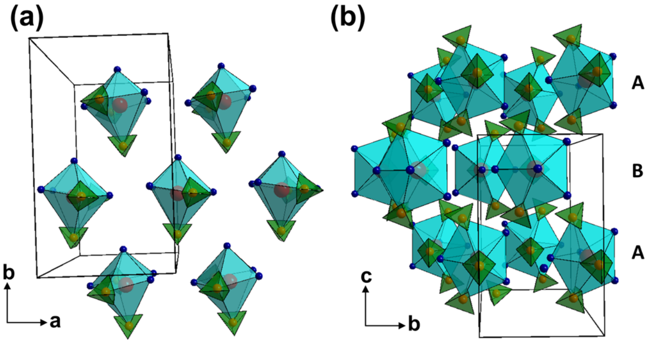

Figure 4. Orthorhombic crystal structure of $M(BH_4)_3{\cdot}4NH_3$ (M = Y, Gd, and Dy) with space group symmetry $Pna2_1$. M^{3+} (red) is coordinated by four N (blue) in NH_3 and three BH_4^- (green tetrahedra), providing neutral molecular complexes $[M(NH_3)_5(BH_4)_3]$ (blue octahedra). (a) $[M(NH_3)_5(BH_4)_3]$ complexes are ordered in hexagonal patterns in the *ab* plane, (b) which are stacked in the order *ABAB* along the *c* direction. H atoms are not shown for simplicity.

$Y(BH_4)_3{\cdot}2NH_3$. $Y(BH_4)_3{\cdot}2NH_3$ crystallizes in an orthorhombic unit cell with space group *Pbca* (No. 61). Y^{3+} is coordinated by two NH_3 and four BH_4^- groups forming an octahedron, where two BH_4^- complexes are bridging to other yttrium atoms (Figure 5). The bridging BH_4^- tetrahedra coordinate to the

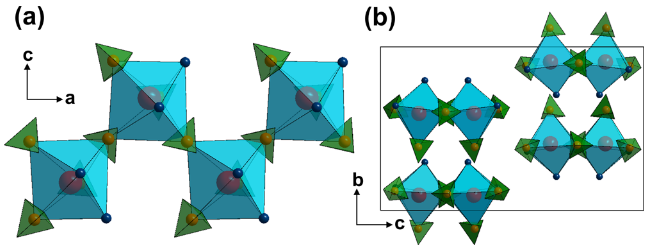

Figure 5. Orthorhombic crystal structure of $Y(BH_4)_3{\cdot}2NH_3$ with space group symmetry *Pbca*. (a) Y^{3+} (red) is coordinated octahedrally (blue octahedra) by two N (blue) in NH_3, to two binding BH_4^- (green tetrahedra), and to two terminal BH_4^- (green tetrahedra) forming a one-dimensional zigzag chain along the *a* axis. (b) Packing of the chains in the unit cell is shown along the [100] direction.

metals via edge sharing (η^2), while the terminal BH_4^- groups coordinate via face sharing (η^3). Thus, the solid $Y(BH_4)_3{\cdot}2NH_3$ consists of one-dimensional zigzag ribbons running along the *a* axis (Figure 5a). All DFT-optimized unit cell parameters vary within 1% from the experimental values, demonstrating a good agreement between the experimental and the optimized structural models.

$Y(BH_4)_3{\cdot}NH_3$. $Y(BH_4)_3{\cdot}NH_3$ crystallizes in an orthorhombic unit cell with space group $Cmc2_1$ (No. 36). Y^{3+} is coordinated by one NH_3 and five BH_4^- complexes, where four BH_4^- tetrahedra are bridging other yttrium atoms by edge sharing (η^2) (Figure 6) and the terminal BH_4^- coordinates via face sharing (η^3). The four bridging BH_4^- groups and Y^{3+} cations create two-dimensional "chess-like" layers in the *ab* plane (Figure 6a), stacked in the *ABAB* order along the *c* axis with terminal BH_4^- and NH_3 placed between the layers (Figure 6b) and stabilizing the structure by a network of dihydrogen $H^{\delta-}\cdots H^{\delta+}$ contacts. Similar layers are observed in the structure of $Sr(BH_4)_2{\cdot}2NH_3$, where they are stacked in the sequence *AAA*.[36] The DFT optimization reorients the NH_3 ligands into a slightly more stable position, but the structural backbone is preserved.

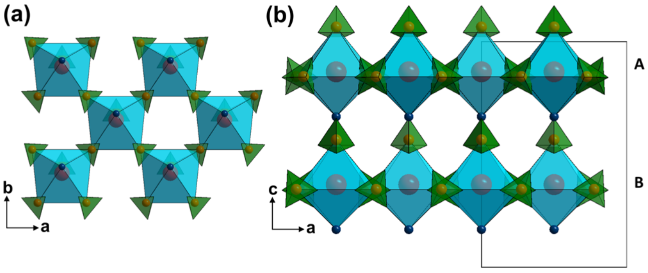

Figure 6. Orthorhombic crystal structure of $Y(BH_4)_3{\cdot}NH_3$ with space group symmetry $Cmc2_1$. Y^{3+} (red) is coordinated by one N (blue) atom in NH_3, to one terminal BH_4^- (green tetrahedra), and to four bridging BH_4^- groups (green tetrahedra). This provides two-dimensional layers in the *ab* plane (a), which are stacked in the order *ABAB* along the *c* axis (b). H atoms are not shown for simplicity.

Comparison of the $M(BH_4)_3{\cdot}nNH_3$ (M = Y, Gd, and Dy) Structures. Two similar polymorphs are known for yttrium borohydride, α-$Y(BH_4)_3$ ($Pa3$) and β-$Y(BH_4)_3$ ($Fm3c$), with β-$Y(BH_4)_3$ being 4.6% less dense as compared to α-$Y(BH_4)_3$.[30,37−41] They both have a ReO_3-type structure and consist of three-dimensional networks of $[Y(BH_4)_6]$ octahedra where each BH_4^- bridges two yttrium atoms by edge (η^2) coordination. Introduction of one or two ammonia molecules interrupts this framework, resulting in yttrium−borohydride that forms two- or one-dimensional layers or chains in the structures of $Y(BH_4)_3{\cdot}NH_3$ and $Y(BH_4)_3{\cdot}2NH_3$, respectively.

Ammine yttrium borohydrides $Y(BH_4)_3{\cdot}nNH_3$ form ionic complexes for $n = 6$ and 7 $[M(NH_3)_n](BH_4)_3$, while molecular structures are obtained for $n = 4$ and 5 $[M(NH_3)_n(BH_4)_3]$. Generally, NH_3 coordinates more strongly than the BH_4^- complexes, and all Y−N bond lengths are in a relatively narrow range of 2.40−2.58 Å. On the other hand, BH_4^- has a more flexible coordination to yttrium observed as varying Y−B distances depending on the coordination number, η^x, i.e., Y−B ≈ 2.5 Å (η^3) for $n = 1$, 2; Y−B ≈ 2.8 Å (η^2) for $n = 0$, 1, 2, and 4; Y−B ≈ 3.1 Å (η^1) for $n = 5$; and Y−B is in the range from 4 to 5 Å for BH_4^- with dominantly ionic interaction with ammine yttrium complexes (η^0) for $n = 6$ and 7 (see Table 3). Thus, the borohydride complex has a flexible coordination to yttrium, i.e., either terminal or bridging ligand, or it acts as counterion. In contrast, NH_3 is always a terminal ligand with a yttrium−nitrogen bond length Y−N ≈ 2.5 Å (η^1) for all structures. The number of NH_3 and BH_4^- ligands coordinating yttrium varies from 6 to 8, while the number of atoms in the first coordination sphere varies from 6 to 12, where it is 12 for $Y(BH_4)_3$, $n = 0$.

Dihydrogen Bonds in the Structures. All ammine yttrium borohydride structures of $Y(BH_4)_3{\cdot}nNH_3$ ($n = 7$, 6, 5, 4, 2, and 1) have dihydrogen $H^{\delta-}\cdots H^{\delta+}$ contacts between partly positively charged hydrogen, $H^{\delta+}$, bonded to N (NH_3) and partly negatively charged hydrogen, $H^{\delta-}$, bonded to B (BH_4). Interestingly, the shortest contacts appear always to be *intermolecular*, either connecting layers ($n = 1$), chains ($n = 2$), molecular clusters ($n = 4$ and 5), or complex ions, $[Y(NH_3)_n]^{3+}$ and BH_4^- ($n = 6$ and 7). The dihydrogen bonds are in the range from 1.850 to 2.029 Å, and an overview is provided in Table 4.

Table 3. Overview of the Coordination of Yttrium, CN(Y), and Selected Bond Lengths for $Y(BH_4)_3{\cdot}nNH_3$[a]

	$n = 0$[b]	$n = 0$[c]	$n = 1$	$n = 2$	$n = 4$	$n = 5$	$n = 6$	$n = 7$
CN(Y)[d]	6	6	6	6	7	8	6	7
CN(Y)[e]	12	12	12	12	10	8	6	7
structure type	3D framework	3D framework	2D layers	1D chains	molecular	molecular	ionic complexes	ionic complexes
Y−N			2.48	2.51	2.44−2.49	2.40−2.58	2.47−2.48	2.47−2.51
Y−B1	2.74 (η^2)	2.75 (η^2)	2.50 (η^3)	2.53(η^3)	2.80 (η^2)	3.13 (η^1)	5.04 (η^0)	4.30 (η^0)
Y−B2	2.75 (η^2)		2.77 (η^2)	2.53(η^3)	2.80 (η^2)		5.15 (η^0)	4.69 (η^0)
Y−B3			2.80 (η^2)	2.79 (η^2)	2.83 (η^2)		5.41 (η^0)	4.72 (η^0)
Y−B4				2.80 (η^2)			5.45 (η^0)	4.97 (η^0)

[a] The distances and hapticities of BH_4^- ligands are obtained from the DFT-optimized crystal structures using the experimental unit cell parameters. [b] Bond distances are provided for α-$Y(BH_4)_3$ extracted from ref 37. [c] Bond distances are provided for β-$Y(BH_4)_3$ extracted from ref 37. [d] Number of BH_4^- and NH_3 ligands coordinated to Y. [e] Number of H (from BH_4) and N (from NH_3) atoms coordinated to Y.

Table 4. Overview of Dihydrogen Bonds between Partly Positively Charged Hydrogen, $H^{\delta+}$, Bonded to N and Partly Negatively Charged Hydrogen, $H^{\delta-}$, Bonded to B for $Y(BH_4)_3 \cdot nNH_3$[a]

n	atoms	shortest $H^{\delta-}\cdots H^{\delta+}$ bond (Å)	type of $H^{\delta-}\cdots H^{\delta+}$ bond
7	N−H30···H6−B	1.850	between $[Y(NH_3)_7]^{3+}$ complex and BH_4^- counterion
6	N−H1···H10−B	1.854	between $[Y(NH_3)_6]^{3+}$ complex and BH_4^- counterion
5	N−H8···H4−B	2.029	intermolecular between $[Y(NH_3)_5(BH_4)_3]$
4	N−H17···H1−B	1.864	intermolecular between $[Y(NH_3)_4(BH_4)_3]$
2	N−H12b···H2a−B	2.033	intermolecular between 1D-chains
1	N−H11b···H1c−B	2.014	intermolecular between 2D-layers

[a] The distances are obtained from the DFT-optimized crystal structures using the experimental unit cell parameters.

For $n = 4$, the shortest dihydrogen bond (1.864 Å) is found within the hexagonal layer, while for $n = 5$, the shortest dihydrogen bond (1.864 Å) is between different layers. Similarly, the shortest dihydrogen contacts in $Mg(BH_4)_2(NH_3BH_3)_2$ (1.995 Å) are also *intermolecular*.[27] However, the two shortest contacts are observed for $Y(BH_4)_3 \cdot nNH_3$ $n = 7$ and 6 (1.850 and 1.854 Å), where BH_4^- units charge balance the complex cations $[Y(NH_3)_n]^{3+}$. For comparison, the intramolecular distances between $H^{\delta-}\cdots H^{\delta-}$ in a BH_4^- tetrahedron and $H^{\delta+}\cdots H^{\delta+}$ in NH_3 are ~2.00 and 1.63 Å, respectively.

Trends in Volume of the Structures. The unit cell volumes per formula unit (V/Z) at RT as a function of the number of ammonia molecules (n) in the compounds, $Y(BH_4)_3 \cdot nNH_3$, are shown in Figure 7. For these ammine yttrium borohydrides, the structural models optimized by DFT calculations reveal a linear increase of unit cell volumes as a function of n, whereas the experimental values deviate from a linear trend. A linear fit to the DFT-calculated V/Z values (dashed line in Figure 7) provides an effective volume per NH_3 of 37.3 Å^3, similar to experimental structures of ammine manganese borohydrides, $Mn(BH_4)_2 \cdot nNH_3$ (n = 0, 2, 3, and 6), 34.0 Å^3 per NH_3. In fact, the latter value, 34.0 Å^3, is identical to the size of the NH_3 molecule in solid NH_3 at −80 °C.[35,42] In general, the best agreement between the experimental and the calculated data is obtained for structures with bridging or edge-sharing BH_4^- complexes.

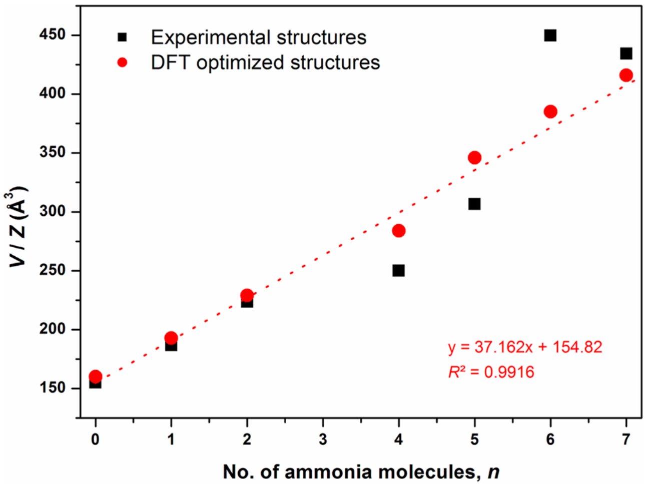

Figure 7. Unit cell volumes (V) at RT divided by the number of formula units (Z) plotted as a function of the number of ammonia molecules in the formula unit, $Y(BH_4)_3 \cdot nNH_3$ (n = 0, 1, 2, 4, 5, 6 and 7). Black squares and red circles correspond to experimental and DFT refined values, respectively. DFT volumes for n = 4 and 5 are extracted from optimizations including van der Waals energies. Red dashed line corresponds to a linear fit based on the DFT-optimized values.

Discrepancies in unit cell volumes (V/Z) for compounds with n = 4, 5, and 6 are observed comparing results from PXD data and DFT optimizations, see Figure 7. This is due to limitations of PXD and static DFT calculations for analysis of solids with a significant degree of dynamics and/or disorder. PXD provides a structural model, which is a static average over time and space of the crystalline solid material. Thus, PXD includes structural dynamics (entropy) in the data but only observable as a deviation, i.e., disorder, from the average static structural model. However, PXD provides valid data on the volume per formula unit of the solid based on experimentally measured data. On the other hand, DFT provides a static structural model obtained by minimizing the total energy, i.e., neglegting entropy contributions.

The molecular structures, n = 4 and 5, reveal volume expansion by DFT structural optimization. The structural energy varies very little upon unit cell volume changes, and multiple local energy minima can be developed by the orientational changes of the BH_4^- and NH_3 groups, possibly because weak interactions, such as dihydrogen bonds, are poorly reproduced by DFT optimizations even though the van der Waals density functional is included.

For the experimental structure of $Y(BH_4)_3 \cdot 6NH_3$, the orientation of the BH_4^- group is disordered in space group Pa-3, whereas it is ordered in the static DFT symmetry $P2_13$. Discrepancy between experimental results from diffraction data and DFT simulations is also previously observed in the scientific literature, possibly for the same reasons. Lithium borohydride exists in two polymorphs, an orthorhombic (LT) o-$LiBH_4$ ($Pnma$), which transforms to a hexagonal (HT) polymorph, h-$LiBH_4$ ($P6_3mc$), at ~110 °C. Negative thermal expansion is observed at the first-order polymorphic transition,[43] and the thermal ellipsoids for boron in the structural model of h-$LiBH_4$ are significantly larger as for o-$LiBH_4$. Hindered rotations of rigid BH_4^- tetrahedra within a set of relatively low-energy barriers in h-$LiBH_4$ may be responsible for the experimental observations. This dynamic disorder may be responsible for the difficulties of DFT in confirming the experimental structure of h-$LiBH_4$ ($P6_3mc$) in contrast to o-$LiBH_4$, which is readily confirmed.[44]

3.3. Solid-State ^{11}B MAS NMR.

The ^{11}B MAS NMR spectrum at 7.05 T of $Y(BH_4)_3 \cdot 7NH_3$ (s1, Figure 8a) reveals a center band at −36.6 ppm (fwhm = 2.6 ppm) along with a small number of spinning side bands (ssb's) from the satellite transitons, covering a spectral width of approximately 100 kHz. Simulation of the satellite transitions, assuming a single ^{11}B site results in the ^{11}B NMR parameters listed in Table 5 and the simulated ssb manifold in Figure 8b. The small value for C_Q indicates that the BH_4^- tetrahedra in s1 are highly symmetric (or mobile at ambient temperature). The envelope of the ssb's

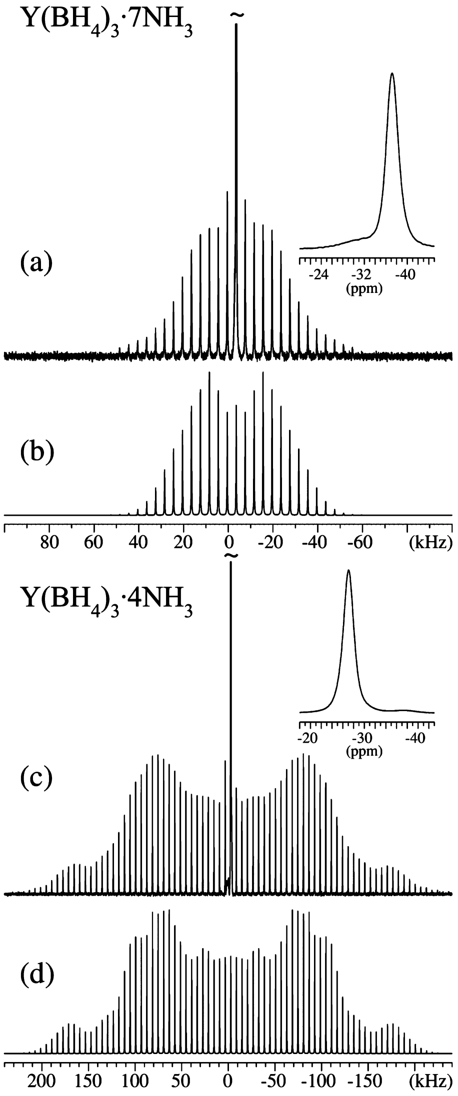

Figure 8. ^{11}B MAS NMR spectra (7.05 T) of (a) $Y(BH_4)_3{\cdot}7NH_3$ (s1) and (c) $Y(BH_4)_3{\cdot}4NH_3$ (s1_165) obtained with spinning speeds of ν_R = 4.0 and 6.0 kHz, respectively. Optimized simulations to the spinning side bands for the satellite transitions are shown in b and d and correspond to the ^{11}B quadrupole coupling (C_Q, η_Q) and isotropic chemical shifts (δ_{iso}) for the two compounds listed in Table 5.

in the experimental spectrum appears to be slightly smeared out compared to the simulation. This feature may reflect minor perturbations of the local environments for the BH_4^- tetrahedra in $Y(BH_4)_3{\cdot}7NH_3$, most likely caused by the presence of multiple ^{11}B sites with nearly identical structural environments and thereby slightly different δ_{iso}, C_Q, and η_Q parameters. Two distinct center band resonances at 14.09 T (Figure 9) are observed at −36.6 and −37.1 ppm, as a result of the increased chemical shift dispersion at higher magnetic field. The structural model determined by SR-PXD data and DFT calculations of $Y(BH_4)_3{\cdot}7NH_3$ reveals the presence of three distinct ^{11}B sites. The structural environments for these BH_4^- sites are very similar (Figure 1), which may explain why three ^{11}B sites are not resolved in the present spectra (Figure 8a). An expansion of the center band resonance for $Y(BH_4)_3{\cdot}7NH_3$ (Figure 9) reveals that the low-frequency peak is much broader than the component at −37.1 ppm. Thus, the spectrum can be interpreted in terms of three sites, where the resonances from two of them coincide at −36.6 ppm.

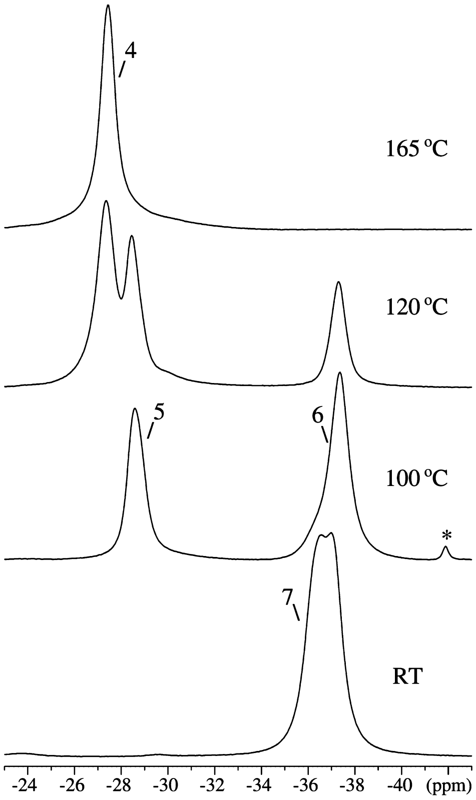

Figure 9. ^{11}B MAS NMR spectra (14.09 T, ν_R = 10.0 kHz) acquired at ambient temperature for $Y(BH_4)_3{\cdot}7NH_3$ before heating (RT) and after heating to 100, 120, and 165 °C, i.e., s1, s1_100, s1_120, and s1_165. By comparing the chemical shifts for n = 7 and 6 with n = 5 and 4, increased chemical shifts are observed for an increase in the covalent character of the bonding between Y and BH_4.

Heat-treatment of $Y(BH_4)_3{\cdot}7NH_3$ at 165 °C (sample s1_165) results in a pure sample of $Y(BH_4)_3{\cdot}4NH_3$, according to PXD (Figure S10, Supporting Information). This is supported by the ^{11}B MAS NMR spectrum at 7.05 T (Figure 8c), which is dominated by a center band resonance at −27.6 ppm with a

Table 5. ^{11}**B NMR Quadrupole Coupling Parameters (**C_Q, η_Q**) and Isotropic Chemical Shifts (**δ_{iso}**) Determined for the** $Y(BH_4)_3{\cdot}nNH_3$ **Series at Ambient Temperature**

sample	δ_{iso} (ppm)	fwhm[a] (ppm)	C_Q (kHz)	η_Q
$Y(BH_4)_3{\cdot}7NH_3$	−36.6 ± 0.2−37.1 ± 0.2		84 ± 10[b]	0.40 ± 10[b]
$Y(BH_4)_3{\cdot}6NH_3$	−37.4 ± 0.2	0.71	n.d.	n.d.
$Y(BH_4)_3{\cdot}5NH_3$	−28.6 ± 0.2	0.79	n.d.	n.d.
$Y(BH_4)_3{\cdot}4NH_3$	−27.5 ± 0.2	0.73	402 ± 20	0.23 ± 0.05

[a] Full width at half-maximum of the center band resonances measured at 14.09 T (Figure 10). [b] Average values for the different ^{11}B sites in $Y(BH_4)_3{\cdot}7NH_3$, obtained from the satellite transitions at 7.05 T.

DOI: 10.1021/acs.inorgchem.5b00951
Inorg. Chem. 2015, 54, 7402−7414

corresponding manifold of ssb's, covering a spectral range of approximately 400 kHz. A small center band resonance from 20 to −3 ppm is also apparent, constituting about 2% of the total center band intensity, which is ascribed to a minor impurity of BO_3 sites arising from a small degree of oxidation during the sample preparation/heat-treatment process. A satisfactory simulation of the ssb's from the satellite transitions can be obtained (Figure 8d), corresponding to the ^{11}B NMR parameters in Table 5. Again, the smeared out appearance of the ssb's in the experimental spectrum may reflect the presence of slightly distorted BH_4^- sites, reflecting that the sample is not highly crystalline or consists of very small crystallites. A narrow center band resonance at −27.5 ppm is also observed at 14.09 T (Figure 9), suggesting that the BH_4^- sites in $Y(BH_4)_3{\cdot}4NH_3$ are structurally very similar when the local geometry of the BH_4^- tetrahedra and the second-coordination spheres are taken into account. This contradicts the previous reported structural model of $Y(BH_4)_3{\cdot}4NH_3$[14] containing two very different chemical environments for BH_4. Hence, this spectrum initiated our new structural model, which is in accord with BH_4^- units coordinating to the metal. The center band resonance at −27.5 ppm is assigned to such units. A reported ^{11}B MAS NMR spectrum at 7.1 T of $Y(BH_4)_3{\cdot}4NH_3$ prepared from $LiBH_4{-}YCl_3{\cdot}4NH_3$ (3:1) contains two types of center band resonances at −28.6 and −39 ppm, where each of these resonances was split into two peaks with no apparent resemblance to the characteristic second-order quadrupolar line shapes, observed for structurally well-defined sites.[12] Comparison of this spectrum with the spectra in Figure 9 suggests that their sample potentially contains a mixture of $Y(BH_4)_3{\cdot}4NH_3$ and $Y(BH_4)_3{\cdot}7NH_3$ or unreacted amorphous $LiBH_4$ accounting for the resonances observed at −28.6 and −39 ppm, respectively.

The stepwise release of ammonia molecules from $Y(BH_4)_3{\cdot}7NH_3$ during heating is investigated in situ by VT-^{11}B MAS NMR at 7.05 T (Figure 10) and ex situ for preheated samples studied at ambient temperature at 14.09 T (Figure 9). The improved resolution at 14.09 T results in a clear observation of four distinct types of resonances, which can be assigned to the different $Y(BH_4)_3{\cdot}nNH_3$ compounds, following PXD analysis of the same samples (Figure S10, Supporting Information). $Y(BH_4)_3{\cdot}6NH_3$ exhibits a slightly lower chemical shift value (−37.4 ppm) than the two resolved resonances observed for $Y(BH_4)_3{\cdot}7NH_3$, reflecting the longer Y−B distances observed for $Y(BH_4)_3{\cdot}6NH_3$ compared to $Y(BH_4)_3{\cdot}7NH_3$ (Table 3). A clear shift to higher frequency of roughly 10 ppm is observed for the n = 5 and 4 forms, which reflects that BH_4^- coordinates to the metal rather than acting as counterions as found for n = 6 and 7. After heating to 100 °C, the spectrum reveals the mutual presence of the n = 5 and 6 compounds and a small fraction of n = 7 (high-frequency shoulder to the n = 6 resonance) and similarly of the n = 4, 5, and 6 compounds after heating to 120 °C. Further information on the transformation from $Y(BH_4)_3{\cdot}7NH_3$ into $Y(BH_4)_3{\cdot}4NH_3$ is achieved from the VT-^{11}B NMR spectra in Figure 10, where the sample is heated stepwise to the indicated temperatures. These spectra show that $Y(BH_4)_3{\cdot}7NH_3$ is stable until at least 64 °C. At 77 °C, a part of $Y(BH_4)_3{\cdot}7NH_3$ has released ammonia and formed both $Y(BH_4)_3{\cdot}6NH_3$ (low-frequency shoulder) and $Y(BH_4)_3{\cdot}5NH_3$. This process continues until 113 °C, where the sample is a mixture of the n = 5, 6, and 7 forms, present in roughly equal amounts. All $Y(BH_4)_3{\cdot}6NH_3$ has transformed into the n = 4 form at 140 °C, where the sample is dominated by n = 4 but still contains small amounts of the n = 5 and 7 compounds.

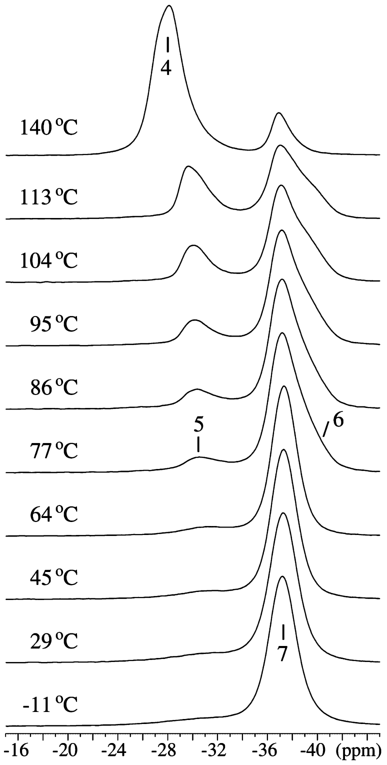

Figure 10. Variable-temperature ^{11}B MAS NMR spectra (7.05 T, ν_R = 4.0 kHz) of $Y(BH_4)_3{\cdot}7NH_3$ (s1), recorded at the indicated temperatures ranging from −11 to 113 °C. In addition, a similar spectrum of the sample heated ex situ to 140 °C (s1_140) is shown above the VT spectra.

In summary, the ^{11}B NMR spectra agree very well with the structural models for n = 7, 6, 5, and 4, and an increase in chemical shifts is observed for an increased covalent character of the bonding between Y and BH_4^-.

3.4. FTIR Spectroscopy. FTIR data measured for $Y(BH_4)_3{\cdot}7NH_3$ and $Y(BH_4)_3{\cdot}4NH_3$ (s1 and s1_165, respectively) are shown in Figure S11, Supporting Information. The spectrum for $Y(BH_4)_3{\cdot}7NH_3$ contains bands from N−H stretch (3311, 3249, 3167, 3204 cm^{-1}), B−H stretch (2242, 2431 cm^{-1}),[45] N−H bend (1601, 1417 cm^{-1}), B−H bend (1232, 1159, 1093 cm^{-1}), and Y−N (580 cm^{-1}). The main difference between $Y(BH_4)_3{\cdot}7NH_3$ and $Y(BH_4)_3{\cdot}4NH_3$ is the B−H bands, 2435 (stretch) and 1159 cm^{-1} (bend), that appear for $Y(BH_4)_3{\cdot}4NH_3$, which may reflect the BH_4^- group coordinated directy to Y. Thus, the FTIR spectra are in accord with the structural models. The FTIR data for $M(BH_4)_3{\cdot}7NH_3$ (M = Y, Gd, and Dy) (Figure S12, Supporting Information) are very similar, in accord with the compounds being isostructural.

3.5. In-Situ SR-PXD of $M(BH_4)_3{\cdot}7NH_3$ (M = Y, Gd, and Dy). In-situ SR-PXD experiments have been conducted for $Y(BH_4)_3{\cdot}7NH_3$, $Gd(BH_4)_3{\cdot}7NH_3$, and $Dy(BH_4)_3{\cdot}7NH_3$ (s1, s2, and s3, respectively) and $Y(BH_4)_3{\cdot}7NH_3{-}Y(BH_4)_3$ (3:4), s4−$Y(BH_4)_3$ (2:2), and $Y(BH_4)_3{\cdot}7NH_3{-}Y(BH_4)_3$ (1:6) (s5, s6, and s7, respectively) from RT to ~300 °C (5 °C/min). Table 6 gives an overview of the results obtained from the in-situ SR-PXD experiments for all samples.

At RT, Bragg reflections are observed from $Y(BH_4)_3{\cdot}7NH_3$ and weak reflections from $Y(BH_4)_3{\cdot}5NH_3$ for s1 (Figure 11). All reflections from $Y(BH_4)_3{\cdot}7NH_3$ disappear in the temperature range from 50 to 90 °C, and reflections from $Y(BH_4)_3{\cdot}6NH_3$ appear at ~50 °C and reach a maximum in intensity

Table 6. Overview of the Samples Investigated by in-Situ SR-PXD, Heated in an Argon Atmosphere with a Rate of 5 °C/min

sample	compounds	T_{form} (°C)^a	T_{max} (°C)^b
s1	$Y(BH_4)_3{\cdot}7NH_3$	RT	90
	$Y(BH_4)_3{\cdot}6NH_3$	50	100
	$Y(BH_4)_3{\cdot}5NH_3$	60	125
	$Y(BH_4)_3{\cdot}4NH_3$	105	170
s2	$Gd(BH_4)_3{\cdot}7NH_3$	RT	80
	$Gd(BH_4)_3{\cdot}6NH_3$	70	100
	$Gd(BH_4)_3{\cdot}5NH_3$	70	120
	$Gd(BH_4)_3{\cdot}4NH_3$	115	180
s3	$Dy(BH_4)_3{\cdot}7NH_3$	RT	70
	$Dy(BH_4)_3{\cdot}6NH_3$	65	95
	$Dy(BH_4)_3{\cdot}5NH_3$	65	115
	$Dy(BH_4)_3{\cdot}4NH_3$	115	180
s5	$Y(BH_4)_3{\cdot}4NH_3$	RT	175
	$Y(BH_4)_3{\cdot}5NH_3$	RT	105
s6	α-$Y(BH_4)_3$	RT	150
	$Y(BH_4)_3{\cdot}4NH_3$	RT	150
	$Y(BH_4)_3{\cdot}2NH_3$	120	165
s7	α-$Y(BH_4)_3$	RT	230
	β-$Y(BH_4)_3$	RT	230
	$Y(BH_4)_3{\cdot}2NH_3$	RT	110
	$Y(BH_4)_3{\cdot}NH_3$	70	175
	u1^c	70	210

$^a T_{\mathrm{form}}$ denotes the formation temperature during heating, i.e., the onset of observed diffraction. $^b T_{\mathrm{max}}$ is the highest temperature where the crystalline compound is observed. ^{c}u1 denotes an unidentified compound.

at ~85 °C before they disappear at ~100 °C (Figure 11b and 11c). The weak reflections from $Y(BH_4)_3{\cdot}5NH_3$ observed at RT remain constant in intensity before they increase at 60 °C and disappear again at 125 °C. When reflections from $Y(BH_4)_3{\cdot}5NH_3$ disappear, new reflections from $Y(BH_4)_3{\cdot}4NH_3$ emerge in the range from 105 to 170 °C. At 170 °C, all reflections disappear and the sample becomes amorphous. When the reflections from $Y(BH_4)_3{\cdot}7NH_3$ decrease in intensity both $Y(BH_4)_3{\cdot}6NH_3$ and $Y(BH_4)_3{\cdot}5NH_3$ increase in intensity (Figure 12c), in accord with in-situ ^{11}B NMR (Figure 10). In fact, s1 has been characterized by in-situ SR-PXD from RT to 200 °C (5 °C/min) in an argon atmosphere three times, but the formation of $Y(BH_4)_3{\cdot}6NH_3$ has only been observed once (Figure 11). For the two other experiments, $Y(BH_4)_3{\cdot}7NH_3$ has been heated in closed capillaries, giving rise to higher partial pressures of ammonia, and the disappearance of $Y(BH_4)_3{\cdot}7NH_3$ is then followed directly by the formation of $Y(BH_4)_3{\cdot}5NH_3$ (Figures S13 and S14, Supporting Information). Similar decomposition mechanisms are observed for s2 ($Gd(BH_4)_3{\cdot}7NH_3$) and s3 ($Dy(BH_4)_3{\cdot}7NH_3$), see Table 6 and Figures S15–S17, Supporting Information.

In summary, the in-situ SR-PXD data reveal that $M(BH_4)_3{\cdot}7NH_3$ (M = Y, Gd, and Dy) release one equivalent of NH_3 in three steps upon thermal treatment, according to reaction 3, which is also in agreement with in-situ ^{11}B NMR.

$$\begin{aligned}&[M(NH_3)_7](BH_4)_3(s)\\ &\quad\rightarrow [M(NH_3)_6](BH_4)_3(s) + NH_3(g)\\ &\quad\rightarrow [M(NH_3)_5(BH_4)_3](s) + 2NH_3(g)\\ &\quad\rightarrow [M(NH_3)_4(BH_4)_3](s) + 3NH_3(g)\end{aligned} \tag{3}$$

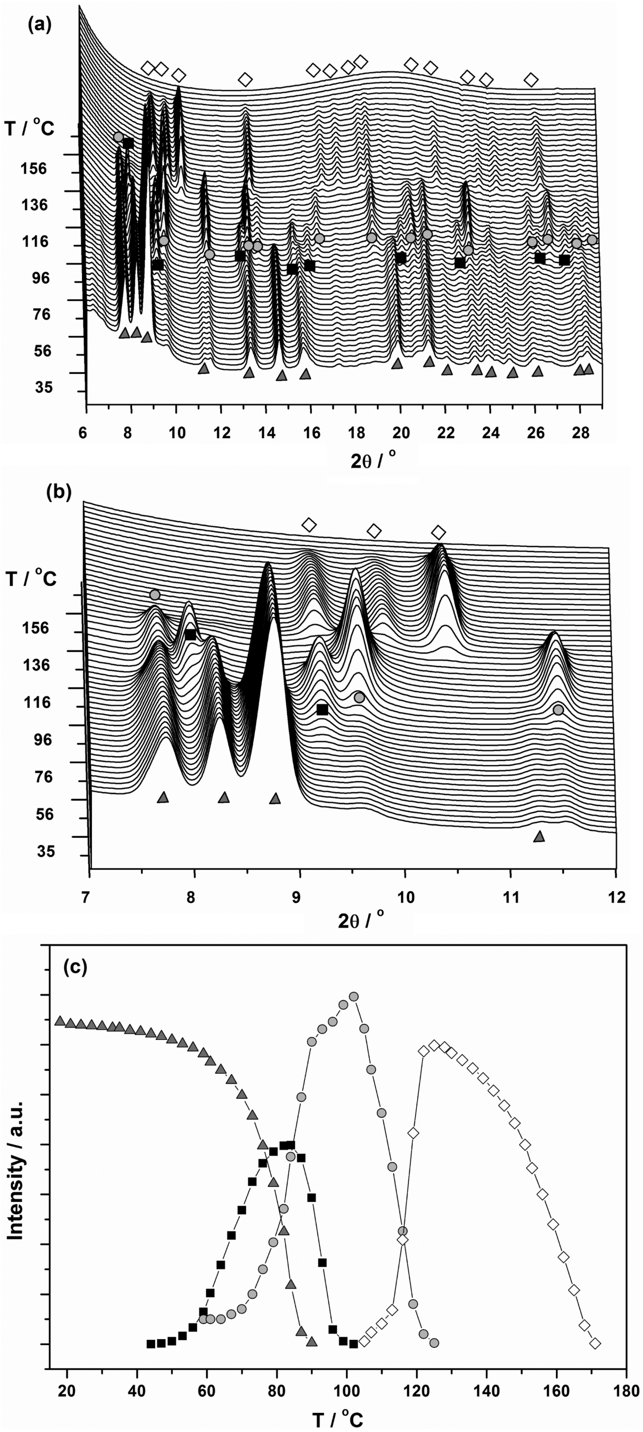

Figure 11. (a) In-situ SR-PXD for $Y(BH_4)_3{\cdot}7NH_3$ (s1) measured from RT to 200 °C (5 °C/min, p(Ar) = 1 bar, λ = 0.99102 Å). (b) Expansion of the in-situ SR-PXD data in the 2θ range from 7° to 12°. (c) Integrated intensities for selected reflections. Symbols: (▲) $Y(BH_4)_3{\cdot}7NH_3$; (■) $Y(BH_4)_3{\cdot}6NH_3$; (●) $Y(BH_4)_3{\cdot}5NH_3$; (◇) $Y(BH_4)_3{\cdot}4NH_3$.

In-situ SR-PXD data collected for s7 ($Y(BH_4)_3$ and $Y(BH_4)_3{\cdot}2NH_3$) from RT to 250 °C are shown in Figure S18a, Supporting Information, while selected integrated Bragg reflections are plotted as a function of the temperature in Figure S18b. In the temperature range from 65 to 110 °C, the reflections from $Y(BH_4)_3{\cdot}2NH_3$ decrease in intensity and finally disappear, while the reflections from α- and β-$Y(BH_4)_3$ only

DOI: 10.1021/acs.inorgchem.5b00951
Inorg. Chem. 2015, 54, 7402−7414

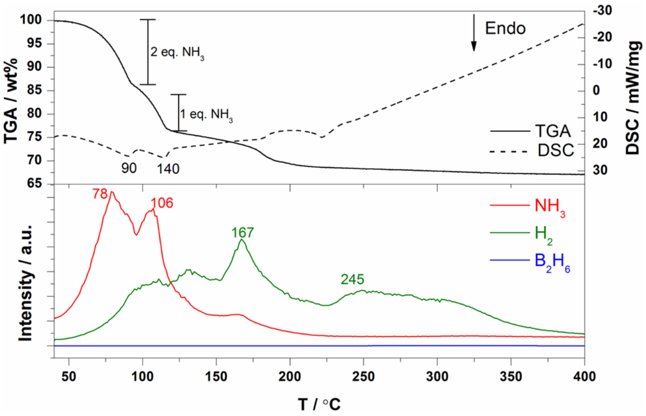

Figure 12. (Top) TGA/DSC for $Y(BH_4)_3$·$7NH_3$ (s1) heated from RT to 400 °C (5 °C/min, argon flow, 20 mL/min). (Bottom) MS signals. NH_3, H_2, and B_2H_6 are presented by red, green, and blue lines, respectively.

decrease in intensity. This results in the formation of $Y(BH_4)_3$·NH_3 and a small amount of an unidentified compound denoted u1 (d = 7.09, 4.65 Å). Reflections from $Y(BH_4)_3$·NH_3 disappear in the temperature range from 115 to 180 °C, which causes an increase in intensity of the peaks from α- and β-$Y(BH_4)_3$. The weak reflections from u1 disappear between 175 and 225 °C, while α- and β-$Y(BH_4)_3$ finally disappear at 230 °C, yielding an amorphous product, which may be $Y(B_3H_8)$.[46,47]

$Y(BH_4)_3$·NH_3 is formed from α- and β-$Y(BH_4)_3$ and $Y(BH_4)_3$·$2NH_3$ upon thermal treatment (for s7). Similarly, $Y(BH_4)_3$·$2NH_3$ is formed from α-$Y(BH_4)_3$ and $Y(BH_4)_3$·$4NH_3$ (s6) as revealed by in-situ SR-PXD (Figure S19, Supporting Information). Here, reflections from $Y(BH_4)_3$·$2NH_3$ decrease in intensity and disappear finally between 150 and 165 °C without the appearance of new peaks.

The composition of the unidentified compound u1 may be the remaining triammine yttrium borohydride, $Y(BH_4)_3$·$3NH_3$. However, attempts to index the structure have been unsuccessful due to the presence of only a few Bragg reflections. $Y(BH_4)_3$·$3NH_3$ will contain six ligands, and yttrium prefers octahedral coordination as in $Y(BH_4)_3$, $[Y(BH_4)_6]$. Thus, the ligands cannot be shared, and the structure will be molecular, $[Y(BH_4)_3(NH_3)_3]$, built from isolated octahedra linked by dihydrogen bonds similar to $M(BH_4)_2$·$4NH_3$ (M = Ca and Sr).[36]

3.6. Thermal Analysis and Temperature-Programmed Photographic Analysis.

Thermogravimetric analysis, differential scanning calorimetry, and simultaneous mass spectrometry (TGA/DSC-MS) data have been collected for $M(BH_4)_3$·$7NH_3$, M = Y, Gd, and Dy (s1, s2, and s3, respectively) from RT to ~400 °C (5 °C/min). The TGA data for s1 (Figure 12) reveal a mass loss of 25 wt % in two steps between RT and 130 °C, and the DSC data show two endothermic events at 90 and 114 °C. The mass loss of 25 wt % is slightly higher than the theoretical weight fraction of three NH_3 molecules (20.2 wt %). This is in accord with the MS data and reflects that not only NH_3 but also H_2 is released below 130 °C. In the temperature range from 150 to 225 °C, a mass loss of 6.5 wt % is observed and an exothermic event is apparent by the DSC data in the same temperature range. The MS data reveal that mainly hydrogen with a maximum at 167 °C and smaller amounts of NH_3 are released. This is similar to the decomposition of YCl_3·$4NH_3$–$LiBH_4$ (1:3) described recently.[14] The exothermic decomposition may reflect that hydrogen is released by dihydrogen elimination from partly positive and partly negative hydrogen atoms from NH_3 and BH_4, respectively. Above 225 °C mainly hydrogen with small amounts of diborane is released (Figure S22, Supporting Information). In accord with the in-situ SR-PXD data, the TGA/DSC-MS data obtained for $Gd(BH_4)_3$·$7NH_3$ (s2) and $Dy(BH_4)_3$·$7NH_3$ (s3) show similar decomposition paths as for $Y(BH_4)_3$·$7NH_3$ (s1) (Figures S21 and S22, Supporting Information). The temperature for the maximum NH_3 release for the first step is at 62 °C for $Dy(BH_4)_3$·$7NH_3$ and at 78 and 82 °C for $Y(BH_4)_3$·$7NH_3$ and $Gd(BH_4)_3$·$7NH_3$, respectively (Figure S22, Supporting Information), suggesting that $Dy(BH_4)_3$·$7NH_3$ is less stable compared to $Y(BH_4)_3$·$7NH_3$ and $Gd(BH_4)_3$·$7NH_3$.

The thermal analysis data for the mixed samples, $Y(BH_4)_3$·$7NH_3$–$Y(BH_4)_3$ (3:4, s5 n/m = 3/3) s4–$Y(BH_4)_3$ (2:2, s6, n/m = 2/3) and $Y(BH_4)_3$·$7NH_3$–$Y(BH_4)_3$ (1:6, s7, n/m = 1/3), are shown in Figure 13. Sample s5 (n/m = 3/3) releases a similar amount of NH_3 compared to $Y(BH_4)_3$·$4NH_3$, while ammonia release is almost suppressed for s6 (n/m = 2/3) and s7 (n/m = 1/3). Thus, hydrogen purity is increased by lowering the n/m ratio. $Y(BH_4)_3$·$7NH_3$–$Y(BH_4)_3$ (1:6, s7, 10.1 wt % H_2) decomposes in three distinct steps upon thermal treatment below 350 °C. First, approximately 1.5 wt % H_2 is released in the temperature range from RT to 135 °C, second about 2.5 wt % H_2 is released from 135 to 190 °C, and finally approximately 4.5 wt % H_2 is released from 190 to 350 °C. $Y(BH_4)_3$·$7NH_3$–$Y(BH_4)_3$ (2:5, s6, 10.8 wt % H_2) has similarly a mass loss of 9.5 wt % between 100 and 350 °C; however, the hydrogen release reactions are less distinct. $Y(BH_4)_3$·$7NH_3$–$Y(BH_4)_3$ (3:4, s5, 11.5 wt % H_2) has a mass loss of 4 wt %,

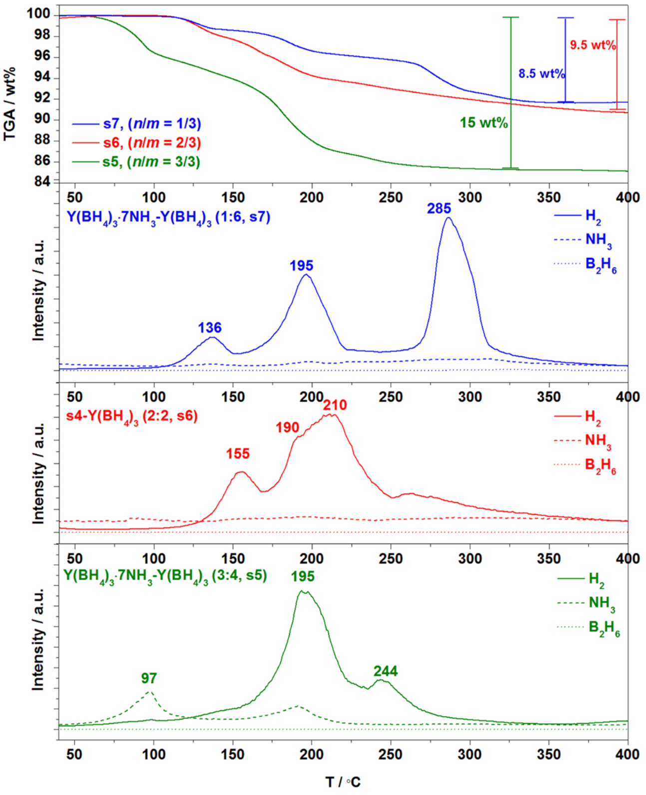

Figure 13. TGA-MS data for $Y(BH_4)_3$·$7NH_3$–$Y(BH_4)_3$ (1:6, s7), s4–$Y(BH_4)_3$ (2:2, s6), and $Y(BH_4)_3$·$7NH_3$–$Y(BH_4)_3$ (3:4, s5) heated from RT to 400 °C (5 °C/min, argon flow, 20 mL/min).

resulting from NH_3 release between 50 and 110 °C, while 11 wt % is released between 125 and 300 °C consisting of a mixture of NH_3 and H_2.

The samples, $M(BH_4)_3{\cdot}7NH_3$, M = Y, Gd, and Dy, have also been studied by temperature-programmed photographic analysis (TPPA) from RT to 300 °C ($\Delta T/\Delta t = 3$ °C/min).[29] Sample s1 is a white powder at RT which becomes slightly darker upon heating (Figure S23, Supporting Information), but it neither melts nor foams during heating. A similar behavior is observed for s2 and s3 (Figures S24 and S25, Supporting Information), which is in contrast to, for example, $Mn(BH_4)_2{\cdot}2NH_3$ that melts at 77 °C.[35]

3.7. Trends in Gas Release and Dihydrogen Bonds.

Ammine metal borohydrides have recently received significant attention owing to their promising hydrogen storage performance. Ammonia is detrimental for low-temperature fuel cells, and the NH_3/BH_4^- ratio (n/m) in $M(BH_4)_m{\cdot}nNH_3$ compounds requires tailoring to avoid ammonia release. In the present work, it is demonstrated that the n/m ratio can be adjusted by mechanochemical treatment of $Y(BH_4)_3{\cdot}7NH_3$–$Y(BH_4)_3$ in various ratios. After mechanochemical treatment of $Y(BH_4)_3{\cdot}7NH_3$–$Y(BH_4)_3$ (3:4, 2:5, and 1:6), mixtures of $Y(BH_4)_3{\cdot}4NH_3$, $Y(BH_4)_3{\cdot}2NH_3$, and $Y(BH_4)_3$ are produced. This is in contrast to mixtures of $M(BH_4)_2{\cdot}6NH_3$–$M(BH_4)_2$ (M = Mg or Mn) that produce single-phase samples with compositions $M(BH_4)_2{\cdot}nNH_3$ (n = 1, 2, or 3).[35,48] For $n/m < 1$, H_2 with minor traces of NH_3 is released rather than mainly NH_3 as observed for $Y(BH_4)_3{\cdot}7NH_3$.

An impirical relation between decomposition temperature and the electronegativity of the metal that coordinates to BH_4^- has been established.[49] Destabilization is observed for most metal borohydrides with low electronegativity ($\chi_p < 1.6$), whereas metal borohydrides with high electronegativity ($\chi_p > 1.6$) are stabilized by NH_3, and strong dihydrogen bonds are proposed to lead to dihydrogen elimination.[4,35] However, our experimental results disagree with that hypothesis. NH_3 is released for $Y(BH_4)_3{\cdot}nNH_3$ (n = 7 and 6), which reveals the strongest dihydrogen bonds (~1.85 Å) among the $Y(BH_4)_3{\cdot}nNH_3$ (n = 7, 6, 5, 4, 2, and 1) compounds. Similarly, $NaBH_4{\cdot}2H_2O$ melts at ~40 °C and then, upon further heating, slowly reacts and releases hydrogen at $T > 40$ °C.[50] Thus, the hydrate $NaBH_4{\cdot}2H_2O$ does not directly release hydrogen but decomposes into anhydrous $NaBH_4$ and water despite the presence of strong dihydrogen bonds. In general, release of ammonia or hydrogen appears not to be determined by the crystal structure, i.e., the strength of the dihydrogen bonds. $Y(BH_4)_3{\cdot}nNH_3$ (n = 4 and 5) both consist of molecular compounds $[Y(NH_3)_n(BH_4)_3]$, where NH_3 and BH_4^- groups coordinate to the metal. However, only NH_3 is released for n = 5, while a mixture of H_2 and NH_3 is released for n = 4. $M(BH_4)_3{\cdot}6NH_3$ (M = Al and Y) both have crystal structures built of complex cations $[M(NH_3)_6]^{3+}$ and are charge balanced by BH_4^-.[51] Hydrogen with traces of ammonia and only ammonia is released for M = Al and Y, respectively.[52]

Similar to $Y(BH_4)_3$, YCl_3 absorbs seven molecules of ammonia forming $YCl_3{\cdot}7NH_3$. However, in contrast to $Y(BH_4)_3{\cdot}7NH_3$, $YCl_3{\cdot}7NH_3$ releases ammonia, producing $YCl_3{\cdot}nNH_3$ (n = 4, 3, 2, and 1) upon heat treatment.[14] This work is the first study to report an extensive series of varying numbers of neutral ligands, n = 7, 6, 5, 4, 2, and 1. Thus, the combination of mechanochemistry and thermal treatment may be a new approach in coordination chemistry for producing complexes with varying numbers of neutral ligands and counterions in the solid state.

■ CONCLUSION

New synthesis methods along with knowledge on the structural, physical, and chemical properties are required to open new possibilities for rational materials design and tailoring materials properties. In the present work, new synthesis approaches have been developed and used to produce three new series of solvent- and halide-free ammine rare-earth metal borohydrides, $M(BH_4)_3{\cdot}nNH_3$ (M = Y, Gd, and Dy; n = 7, 6, 5, 4, 2, and 1). $M(BH_4)_3$ absorbs seven ammonia molecules, $M(BH_4)_3{\cdot}7NH_3$, that stepwise releases ammonia, producing $M(BH_4)_3{\cdot}nNH_3$ (n = 6, 5, and 4), as revealed by in-situ SR-PXD and in-situ VT ^{11}B MAS NMR. The NH_3/BH_4^- ratio for $Y(BH_4)_3{\cdot}nNH_3$ has been tailored by mechanochemical treatment of $Y(BH_4)_3{\cdot}7NH_3$–$Y(BH_4)_3$ in various ratios, giving $Y(BH_4)_3{\cdot}nNH_3$ (n = 2 and 1), which effectively increases the hydrogen purity of the released gas. This synthesis route may represent a new approach in coordination chemistry for producing complexes with varying numbers of neutral ligands and counterions in the solid state. Crystal structural models have been derived from a combination of SR-PXD, ^{11}B MAS NMR, and DFT calculations. NH_3 acts as a terminal ligand in all structures, while the borohydride complex has a flexible coordination, i.e., the BH_4^- complex acts as either a terminal or a bridging ligand or as a counterion. This is reflected in the solid-state ^{11}B MAS NMR spectra, where an increase in chemical shifts is observed for an increased covalent character of the bonding between Y and BH_4^-. Disorder and/or dynamics are observed in structures of $M(BH_4)_3{\cdot}nNH_3$ (n = 6 and 5), which is discussed and illustrates limitations of the complementary methods of PXD and DFT. This kind of knowledge on trends in structures and properties is vital for the design of new materials with specific properties.

■ ASSOCIATED CONTENT

Ⓢ Supporting Information

Rietveld refinements, crystallographic data in CIF format, additional thermal analysis data, and FTIR spectra. The Supporting Information is available free of charge on the ACS Publications website at DOI: 10.1021/acs.inorgchem.5b00951.

■ AUTHOR INFORMATION

Corresponding Author

*E-mail: trj@chem.au.dk.

Notes

The authors declare no competing financial interest.

■ ACKNOWLEDGMENTS

The Danish Council for Strategic Research is acknowledged for financial support to the project HyFillFast. The Danish National Research Foundation is thanked for funding to the Center for Materials Crystallography (CMC, DNRF93) and the Sino-Danish Center for Education and Research (SDC). This research was partially funded by the Swiss National Science Foundation under project 200020_149218. We are grateful to the Swiss-Norwegian Beamline at ESRF, Grenoble; I-11 at Diamond, Oxford; P02 at DESY, Hamburg; and I-711 at MAXlab, Lund for the provision of the beam time. Finally, the use of the facilities at the Instrument Centre for Solid-State NMR Spectroscopy, Aarhus University, sponsored by the Danish Natural Science Research Councils and the Carlsberg Foundation, is acknowledged. Y.-S. Lee acknowledges the helpful discussion of the calculation results with Sung Hoon Hwang.

REFERENCES

(1) Rude, L. H.; Nielsen, T. K.; Ravnsbæk, D. B.; Bösenberg, U.; Ley, M. B.; Richter, B.; Arnbjerg, L. M.; Dornheim, M.; Filinchuk, Y.; Besenbacher, F.; Jensen, T. R. *Phys. Status Solidi A* **2011**, *208*, 1754−1773.

(2) David, W. I. F. *Faraday Discuss.* **2011**, *151*, 399−414.

(3) Orimo, S. I.; Nakamori, Y.; Eliseo, J. R.; Züttel, A.; Jensen, C. M. *Chem. Rev.* **2007**, *107*, 4111−4132.

(4) Jepsen, L. H.; Ley, M. B.; Lee, Y.-S.; Cho, Y. W.; Dornheim, M.; Jensen, J. O.; Filinchuk, Y.; Jørgensen, J. E.; Besenbacher, F.; Jensen, T. R. *Mater. Today* **2014**, *17*, 129−135.

(5) Ley, M. B.; Jepsen, L. H.; Lee, Y.-S.; Cho, Y. W.; Bellosta von Colbe, J. M.; Dornheim, M.; Rokni, M.; Jensen, J. O.; Sloth, M.; Filinchuk, Y.; Jørgensen, J. E.; Besenbacher, F.; Jensen, T. R. *Mater. Today* **2014**, *17*, 122−128.

(6) Filinchuk, Y.; Richter, B.; Jensen, T. R.; Dmitriev, V.; Chernyshov, D.; Hagemann, H. *Angew. Chem., Int. Ed.* **2011**, *50*, 11162−11166.

(7) Ley, M. B.; Ravnsbæk, D. B.; Filinchuk, Y.; Lee, Y.-S.; Janot, R.; Cho, Y. W.; Skibsted, J.; Jensen, T. R. *Chem. Mater.* **2012**, *24*, 1654−1663.

(8) Ley, M. B.; Boulineau, S.; Janot, R.; Filinchuk, Y.; Jensen, T. R. *J. Phys. Chem. C* **2012**, *116*, 21267−21276.

(9) Frommen, C.; Sørby, M. H.; Ravindran, P.; Vajeeston, P.; Fjellvåg, H.; Hauback, B. C. *J. Phys. Chem. C* **2011**, *115*, 23591−23602.

(10) Marks, S.; Heck, J. G.; Habicht, M. H.; Oña-Burgos, P.; Feldmann, C.; Roesky, P. W. *J. Am. Chem. Soc.* **2012**, *134*, 16983−16986.

(11) Schouwink, P.; Ley, M. B.; Tissot, A.; Hagemann, H.; Jensen, T. R.; Smrčok, L′.; Černý, R. *Nat. Commun.* **2014**, *5*, 5706.

(12) Gu, Q.; Gao, L.; Guo, Y.; Tan, Y.; Tang, Z.; Wallwork, K. S.; Zhang, F.; Yu, X. *Energy Environ. Sci.* **2012**, *5*, 7590−7600.

(13) Guo, Y.; Wu, H.; Zhou, W.; Yu, X. *J. Am. Chem. Soc.* **2011**, *133*, 4690−4693.

(14) Yuan, F.; Gu, Q.; Guo, Y.; Sun, W.; Chen, X.; Yu, X. *J. Mater. Chem.* **2012**, *22*, 1061−1068.

(15) Ley, M. B.; Paskevicius, M.; Schouwink, P.; Richter, B.; Sheppard, D. A.; Buckley, C. E.; Jensen, T. R. *Dalton Trans.* **2014**, *43*, 13333−13342.

(16) Jensen, T. R.; Nielsen, T. K.; Filinchuk, Y.; Jørgensen, J.-E.; Cerenius, Y.; Gray, E. M.; Webb, C. J. *J. Appl. Crystallogr.* **2010**, *43*, 1456−1463.

(17) Hammersley, A. P.; Svensson, S. O.; Hanfland, M.; Fitch, A. N.; Hausermann, D. *High Pressure Res.* **1996**, *14*, 235−248.

(18) Boultif, A.; Louër, D. *J. Appl. Crystallogr.* **2004**, *37*, 724−731.

(19) Favre-Nicolin, V.; Černý, R. *J. Appl. Crystallogr.* **2002**, *35*, 734−743.

(20) Rodriguez-Carvajal, J. *FULLPROF SUITE*; LLB Sacley & LCSIM: Rennes, France, 2003.

(21) Spek, A. L. *Acta Crystallogr., Sect. D: Biol. Crystallogr.* **2009**, *65*, 148−155.

(22) Perdew, J. P.; Burke, K.; Ernzerhof, M. *Phys. Rev. Lett.* **1996**, *77*, 3865−3868.

(23) Kresse, G.; Furthmüller, J. *Phys. Rev. B: Condens. Matter Mater. Phys.* **1996**, *54*, 11169−11186.

(24) Blöchl, P. E. *Phys. Rev. B: Condens. Matter Mater. Phys.* **1994**, *50*, 17953−17979.

(25) Lee, K.; Murray, É. D.; Kong, L.; Lundqvist, B. I.; Langreth, D. C. *Phys. Rev. B: Condens. Matter Mater. Phys.* **2010**, *82*, 081101.

(26) Klimeš, J.; Bowler, D. R.; Michaelides, A. *Phys. Rev. B: Condens. Matter Mater. Phys.* **2011**, *83*, 195131.

(27) Jepsen, L. H.; Ban, V.; Møller, K. T.; Lee, Y.-S.; Cho, Y. W.; Besenbacher, F.; Filinchuk, Y.; Skibsted, J.; Jensen, T. R. *J. Phys. Chem. C* **2014**, *118*, 12141−12153.

(28) Skibsted, J.; Nielsen, N. C.; Bildsøe, H.; Jakobsen, H. J. *J. Magn. Reson.* **1991**, *95*, 88−117.

(29) Paskevicius, M.; Ley, M. B.; Sheppard, D. A.; Jensen, T. R.; Buckley, C. E. *Phys. Chem. Chem. Phys.* **2013**, *15*, 19774−19789.

(30) Sato, T.; Miwa, K.; Nakamori, Y.; Ohoyama, K.; Li, H.-W.; Noritake, T.; Aoki, M.; Towata, S. I.; Orimo, S. I. *Phys. Rev. B: Condens. Matter Mater. Phys.* **2008**, *77*, 104114.

(31) Shannon, R. D. *Acta Crystallogr., Sect. A: Cryst. Phys., Diffr., Theor. Gen. Crystallogr.* **1976**, *32*, 751−767.

(32) McCullough, J. D.; Trueblood, K. N. *Acta Crystallogr.* **1959**, *12*, 507−511.

(33) Christensen, A. N.; Nielsen, M.; O'Reilly, K. P. J.; Wroblewski, T.; Niemi, V.; Sandström, J.; Krogsgaard-Larsen, P. *Acta Chem. Scand.* **1992**, *46*, 224−230.

(34) Schwarzmann, S. *Z. Kristallogr.* **1964**, *120*, 286−316.

(35) Jepsen, L. H.; Ley, M. B.; Filinchuk, Y.; Besenbacher, F.; Jensen, T. R. *ChemSusChem* **2015**, *8*, 1452−1463.

(36) Jepsen, L. H.; Lee, Y.-S.; Cerný, R.; Sarusie, R. S.; Cho, Y. W.; Besenbacher, F.; Jensen, T. R. Submitted for publication, 2015.

(37) Ravnsbaek, D. B.; Filinchuk, Y.; Cerny, R.; Ley, M. B.; Haase, D.; Jakobsen, H. J.; Skibsted, J.; Jensen, T. R. *Inorg. Chem.* **2010**, *49*, 3801−3809.

(38) Frommen, C.; Aliouane, N.; Deledda, S.; Fonneløp, J. E.; Grove, H.; Lieutenant, K.; Llamas-Jansa, I.; Sartori, S.; Sørby, M. H.; Hauback, B. C. *J. Alloys Compd.* **2010**, *496*, 710−716.

(39) Jaroń, T.; Koźmiński, W.; Grochala, W. *Phys. Chem. Chem. Phys.* **2011**, *13*, 8847−8851.

(40) Lee, Y.; Shim, J.; Cho, Y. *J. Phys. Chem. C* **2010**, *114*, 12833−12837.

(41) Jaroń, T.; Grochala, W. *Dalton Trans.* **2010**, *39*, 160−166.

(42) Olovsson, I.; Templeton, D. H. *Acta Crystallogr.* **1959**, *12*, 832−836.

(43) Filinchuk, Y.; Chernyshov, D.; Černý, R. *J. Phys. Chem. C* **2008**, *112*, 10579−10584.

(44) Shevlin, S. A.; Cazorla, C.; Guo, Z. X. *J. Phys. Chem. C* **2012**, *116*, 13488−13496.

(45) D'Anna, V.; Spyratou, A.; Sharma, M.; Hagemann, H. *Spectrochim. Acta, Part A* **2014**, *128*, 902−906.

(46) Remhof, A.; Borgschulte, A.; Friedrichs, O.; Mauron, P.; Yan, Y.; Züttel, A. *Scr. Mater.* **2012**, *66*, 280−283.

(47) Yan, Y.; Remhof, A.; Rentsch, D.; Lee, Y.-S.; Whan Cho, Y.; Züttel, A. *Chem. Commun.* **2013**, *49*, 5234−5236.

(48) Yang, Y.; Liu, Y.; Li, Y.; Gao, M.; Pan, H. *Chem. - Asian J.* **2013**, *8*, 476−481.

(49) Züttel, A.; Borgschulte, A.; Orimo, S. I. *Scr. Mater.* **2007**, *56*, 823−828.

(50) Filinchuk, Y.; Hagemann, H. *Eur. J. Inorg. Chem.* **2008**, *20*, 3127−3133.

(51) Tang, Z.; Tan, Y.; Wu, H.; Gu, Q.; Zhou, W.; Jensen, C. M.; Yu, X. *Acta Mater.* **2013**, *61*, 4787−4796.

(52) Guo, Y.; Yu, X.; Sun, W.; Sun, D.; Yang, W. *Angew. Chem., Int. Ed.* **2011**, *50*, 1087−1091.